International Journal of Plasticity 148 (2022) 103148

Contents lists available at ScienceDirect

International Journal of Plasticity

journal homepage: www.elsevier.com/locate/ijplas

Temperature-dependent universal dislocation structures and transition of plasticity enhancing mechanisms of the $Fe_{40}Mn_{40}Co_{10}Cr_{10}$ high entropy alloy

Jin-Kyung Kim [a,*], Ji Hoon Kim [b], Hyojin Park [a], Jin-Seob Kim [a], Guanghui Yang [a], Rosa Kim [a], Taejin Song [c], Dong-Woo Suh [b], Jongryoul Kim [a]

[a] Department of Materials Science and Chemical Engineering, Hanyang University, Ansan 15588, Republic of Korea
[b] Graduate Institute of Ferrous Technology, Pohang University of Science and Technology, Pohang 37673, Republic of Korea
[c] Steel Products Research Group, Technical Research Laboratories, POSCO, Gwangyang 57807, Republic of Korea

ARTICLE INFO

Keywords:
High entropy alloy
Mechanical properties
Transmission electron microscopy (TEM)
Stacking fault energy
Dislocation

ABSTRACT

The FCC $Fe_{40}Mn_{40}Co_{10}Cr_{10}$ (at.%) high entropy alloy exhibits deformation twinning for room temperature deformation and deformation-induced HCP transformation for subzero deformation. Since the systematic investigation of temperature-dependent dislocation structures is not available, we present an in-depth characterization of the defects involved in deformation at room temperature (298 K) and subzero temperature (223 K) of the cold-rolled and annealed $Fe_{40}Mn_{40}Co_{10}Cr_{10}$ alloy. The material deformed at 223 K shows a higher strain hardening rate than the material deformed at room temperature while both materials show large ductility, 48% for the 223 K deformation and 55% for the 298 K deformation. The main deformation mechanisms of the investigated HEA include the development of inhomogeneous dislocation structures and interaction between dislocations and deformation twin/mechanically induced HCP martensite. The stacking fault energy measured using TEM weak-beam dark-field imaging of dissociated dislocations is 20±9 mJ/m^2 at 298 K. The $Fe_{40}Mn_{40}Co_{10}Cr_{10}$ alloy exhibiting a positive temperature dependence of SFE leads to a decrease of SFE as deformation temperature decreases from 298 K to 223 K. The decrease of SFE results in the transition from deformation twinning to deformation-induced HCP transformation. Further, at higher strains at 223 K, kink banding of HCP and reverse transformation from HCP to FCC were observed, which could account for strain accommodation and stress relaxation, and the large ductility. The 298 K deformation leads to various types of dislocation structures: Extended dislocations, Taylor lattice of perfect dislocations, dislocation loops, highly dense dislocation walls, cell blocks, and cell structures. The observed dislocation structures at 298 K and 223 K are similar suggesting the minor effect of SFE on dislocation structures.

1. Introduction

High-entropy alloys (HEA) provide a new alloying strategy of combining multiple principal elements in high concentrations (George et al., 2019). The HEAs have received considerable attention due to limitless compositional space and outstanding mechanical

* Corresponding author.
E-mail address: jinkyungkim@hanyang.ac.kr (J.-K. Kim).

https://doi.org/10.1016/j.ijplas.2021.103148
Received 21 July 2021; Received in revised form 28 October 2021;
Available online 8 November 2021

properties (George et al., 2020, 2019). The equiatomic CoCrFeMnNi alloy has been extensively investigated as a model alloy system (Kaushik et al., 2021; Laplanche et al., 2016; Otto et al., 2013; Wang et al., 2020). Recently, non-equiatomic single-, dual- or multiphase structures have been proposed to increase the flexibility of HEA design and overcome the limitations of the original HEA design concept (Deng et al., 2015; He et al., 2021a; 2021b; Li et al., 2016; Li and Raabe, 2017; Ma et al., 2015; Ming et al., 2018, 2019; Pradeep et al., 2015; Yao et al., 2014).

Strength-ductility balance (Otto et al., 2013) and fracture toughness (Gludovatz et al., 2014) of the equiatomic CoCrFeMnNi HEA at cryogenic temperatures are superior compared to those at room temperature due to activation of deformation twinning. To optimize stacking fault energy (SFE) and transfer the excellent twinning-induced cryogenic mechanical behavior to room temperature, the $Fe_{40}Mn_{40}Co_{10}Cr_{10}$ HEA was designed by adding Mn, removing Ni, and reducing Cr and Co content from the CoCrFeMnNi HEA (Deng et al., 2015). The FCC $Fe_{40}Mn_{40}Co_{10}Cr_{10}$ HEA exhibits low yield strength (YS), large ductility, and high work hardening (Deng et al., 2015; Picak et al., 2019). Deformation mechanisms of the hot-rolled and homogenized $Fe_{40}Mn_{40}Co_{10}Cr_{10}$ alloy are characterized by prevalent dislocation slip by the formation of highly dense dislocation wall (HDDW) and dislocation cell (DC) structures at low strains and simultaneous activation of slip and deformation twinning at high stains (Deng et al., 2015). Picak et al. (2019) investigated the work hardening behavior of the [111], [001], and [123] oriented single crystal $Fe_{40}Mn_{40}Co_{10}Cr_{10}$ alloys and reported strong orientation-dependent deformation twinning and planar slip and orientation-independent dislocation wall/network.

The SFE is a key parameter affecting the deformation mechanisms of FCC materials. Generally, a high SFE promotes cross-slip of dislocations and often leads to the formation of microbands whereas a low SFE leads to planar slip, deformation twinning, and a deformation-induced martensitic transformation. The FCC-based HEAs also show SFE dependent deformation mechanisms, and enhancement of strain hardening by activating deformation twinning (TWIP effect) (Deng et al., 2015; Joo et al., 2017; Laplanche et al., 2016; Otto et al., 2013; Zhang et al., 2020), martensitic transformation (TRIP effect) (Li et al., 2016, 2017), and microbanding (MBIP effect) (Yang et al., 2018). He et al. (2019) investigated mechanical properties and deformation mechanisms of the $Fe_{40}Mn_{40}Co_{10}Cr_{10}$ alloy in the temperature range from 77 K to 298 K. The room temperature deformation was characterized by deformation twinning and slip while the cryogenic deformation led to deformation-induced martensitic transformation, deformation twinning, and slip. The combined contribution of martensitic transformation and twinning upon deformation could contribute to the higher strain hardening behavior at cryogenic temperature than at room temperature.

HEAs exhibit distinct behavior of dislocation slip compared to conventional materials having dilute solutions because local composition variations affect defect energetics and configurations, and hence resistance to dislocation motion and accumulation (Ma, 2020). Previous work indicates that dislocation structures of HEAs evolved from planar slip at small strains to cross-slipped tangled dislocations at intermediate strains and cell structures at high strains (George et al., 2020; Laplanche et al., 2016; Otto et al., 2013). Otto et al. (2013) reported the activation of the dominant planar slip of perfect dislocations at the early stages of plastic deformation of the CoCrFeMnNi alloy at temperatures ranging from 77 K to 1073 K. Laplanche et al. (2016) investigated deformation mechanisms of the CoCrFeMnNi alloy at liquid nitrogen (77 K) temperature and room temperature and reported the formation of dislocation pile-ups at the initial stage of deformation and reorganization into cell structures with higher dislocation densities at around 20% strain. Xu et al. (2018) reported that the room temperature deformation of the $Al_{0.1}CoCrFeNi$ (at.%) HEA exhibited the formation of immobile Lomer-Cottrell dislocation locks from the reactions of dissociated dislocations originating from the low SFE ranging from 6 to 21 mJ/m^2.

The room temperature strain-dependent dislocation structures reported for the low SFE (~20 mJ/m^2) Fe-22Mn-0.6C (wt.%) steel (Gutierrez-Urrutia and Raabe, 2011), the $Fe_{40}Mn_{40}Co_{10}Cr_{10}$ HEA (Deng et al., 2015), and the high SFE (63 mJ/m^2) Fe-30.5Mn-2.1Al-1.2C (wt.%) steel (Gutierrez-Urrutia and Raabe, 2012) showed similar features such as HDDWs, DCs. However, the dislocation evolution of FCC materials upon subzero temperature deformation has not been thoroughly investigated. Previous work for the $Fe_{40}Mn_{40}Co_{10}Cr_{10}$ HEA reported the room temperature strain-dependent dislocation structures and the transition of plasticity enhancing mechanisms from deformation twinning for room temperature deformation to deformation-induced HCP transformation for subzero deformation (Table 2 in Section 3.1). However, the systematic investigation of temperature-dependent dislocation structures is not available. Therefore, we examine the mechanical properties, evolution of dislocation structures, and various plasticity enhancing mechanisms resulting from deformation of the cold-rolled and annealed $Fe_{40}Mn_{40}Co_{10}Cr_{10}$ alloy at 298 and 223 K (25 and −50 °C). The in-depth microstructural characterization focuses on the measurement of SFE, strain-dependent dislocation structures, and activation of various plasticity enhancing mechanisms.

2. Material and methods

The intended chemical composition of the alloy used in the present work is $Fe_{40}Mn_{40}Co_{10}Cr_{10}$ (at.%), and the actual chemical composition of the alloy, measured by inductively coupled plasma (ICP) analysis, is listed in Table 1. The 80 mm thick slabs produced from vacuum cast ingots were solution-treated at 1473 K for 2 h and hot-rolled to a thickness of 3 mm, prior to cold-rolling to a thickness of 1.5 mm. The cold-rolled materials were recrystallization annealed at 900 °C for 1 h and water-quenched to room

Table. 1
Chemical composition of the investigated material.

Element	Fe	Mn	Co	Cr
Composition (at.%)	40.34	39.84	9.94	9.88

temperature.

The present work focused on the characterization of microstructures and mechanical properties of the cold-rolled and annealed materials. Standard ASTM-E8 tensile specimens were machined with their tensile axis parallel to the rolling direction (RD). Tensile tests were performed in a ZWICK Z100 universal tensile testing machine at a strain rate of $10^{-3}\ s^{-1}$ at room temperature and 223 K. Some tensile tests were interrupted at the selected strain levels to observe deformation microstructures.

Phase analysis was conducted by X-ray diffraction (XRD) using a Rigaku D/MAX-2500/PC. Microstructures were characterized by electron backscatter diffraction (EBSD) and transmission electron microscopy (TEM). EBSD and XRD samples were prepared by mechanical polishing, followed by electrolytic polishing with a solution of 5% perchloric acid and 95% acetic acid. An EDAX-TSL detector attached in an FEI Quanta 3D FEG scanning electron microscopy operated at 20 kV was used to collect EBSD patterns. The step size of the EBSD scans was 50 nm. The OIM analysis software was used to analyze EBSD data. TEM samples were prepared as 3 mm diameter disks which were mechanically polished to a thickness less than 100 μm and thinned by an electrolytic double jet technique at room temperature. A mixture of 5% perchloric acid and 95% ethanol was used as an electrolyte. The surface of TEM samples was parallel to the RD-transverse direction (TD) plane and perpendicular to the normal direction (ND) of the cold-rolled material. TEM observations were conducted in a JEOL 2100F FE-TEM operated at 200 kV. The bright-field (BF) images, dark-field (DF) images, weak beam dark-field (WBDF) images, and diffraction patterns (DP) were acquired for TEM characterization. The thickness of twins and HCP phase was measured from BF/DF images using the Digital Micrograph software. To measure the SFE, long dissociated dislocations on their {111} planes were analyzed by the WBDF images taken using (g, 2 g) diffraction conditions.

3. Results

3.1. Mechanical properties and deformation microstructures of $Fe_{40}Mn_{40}Co_{10}Cr_{10}$

The comparison of the engineering stress-strain curves of the investigated material deformed at room temperature and 223 K is provided in Fig. 1(a). The material deformed at room temperature shows a yield strength (YS) of 208 MPa, an ultimate tensile strength (UTS) of 475 MPa, and total elongation (TE) of 55%. The material deformed at 223 K shows higher strength and slightly lower ductility than the material deformed at room temperature, i.e. YS of 246 MPa, UTS of 583 MPa, and TE of 48%. Fig. 1(b) presents the strain hardening rate curves of the investigated material deformed at room temperature and 223 K. The material deformed at 223 K shows a higher strain hardening rate than the material deformed at room temperature. The two strain hardening curves are almost identical at the initial stage of deformation. The curves show a continuous decrease in strain hardening rate with increasing strain, following the dotted line. At 223 K, the decrease of the strain hardening rate deviates from the dotted line (Stage A) at a smaller true strain of 0.09 than 0.17 for the 298 K material (which can account for the lower ductility). Thus, strain hardening has two stages, where stage B indicates a change of deformation mechanisms discussed in Sections 3.3 and 3.4.

EBSD analysis of the annealed material and materials deformed at room temperature is provided in Fig. 2. The EBSD image quality (IQ) map of the annealed material shows a fully recrystallized microstructure with FCC crystal structure (Fig. 2(a_1)). The grain size of the material is approximately 20 μm. The black lines and the red lines in the IQ maps indicate high angle grain boundaries with a misorientation angle larger than 15 ° and Σ3 twin boundaries with a misorientation angle of 60±5 °, respectively. The microstructure shows a high density of annealing twins, which is evidence of recrystallization of a low SFE FCC material (Mahajan et al., 1997). The RD inverse pole figure (IPF) map of the annealed material shows a random grain orientation (Fig. 2(b_1)). The strain-dependent RD IPF

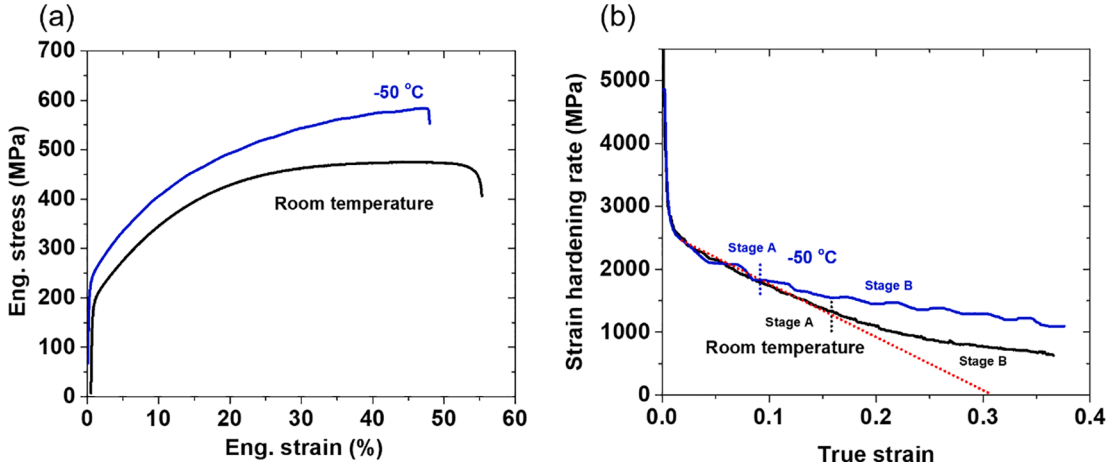

Fig. 1. Mechanical properties of $Fe_{40}Mn_{40}Co_{10}Cr_{10}$. (a) Engineering stress-strain curves of the cold-rolled and annealed $Fe_{40}Mn_{40}Co_{10}Cr_{10}$ (at.%) deformed at 298 and 223 K, indicating higher strength and slightly lower ductility at 223 K. (b) Strain hardening rate curves initially show a continuous decrease in strain hardening rate with increasing strain, following the dotted line. The deviation from the initial hardening rate reflects activation of plasticity enhancing mechanisms (the 223 K oscillations are an artifact of periodic introduction of liquid nitrogen).

maps are shown in Fig. 2(b_1)-(b_3). With increasing deformation level, the random grain orientation changes toward blue ⟨111⟩ and red ⟨100⟩ orientations // tensile direction. The IPFs along the tensile direction clarify the texture change upon deformation (Fig. 2(c)). The sizes of the dots indicate relative grain sizes. This texture change is similar to previous works reported for the $Fe_{40}Mn_{40}Co_{10}Cr_{10}$ HEA (Deng et al., 2015), and high Mn steels (Gutierrez-Urrutia and Raabe, 2011; Kim et al., 2013). The microstructure of the 20% strained material shows thin deformation twins in a few grains as indicated by yellow arrows in Fig. 2(a_2). The microstructure of the 40% strained material shows a higher amount of deformation twins (Fig. 2(a_3)), and some grains show the occurrence of primary twins and secondary twins as indicated by orange arrows. Deng et al. (2015) also observed double twin systems in grains oriented along ⟨111⟩ // tensile direction and twin-free grains oriented along ⟨001⟩ // tensile direction, which is consistent with the present work. Note that the annealing twin boundaries detected in the as-annealed material are mostly not indexed in the 40% strained material as plastic deformation altered misorientation near the annealing twin boundaries.

The XRD patterns and EBSD micrographs of the material deformed at 223 K are provided in Fig. 3. Note that the fracture surface had almost no necking, and the local strain would be similar to the macroscopic fracture strain. The XRD patterns of the undeformed, the

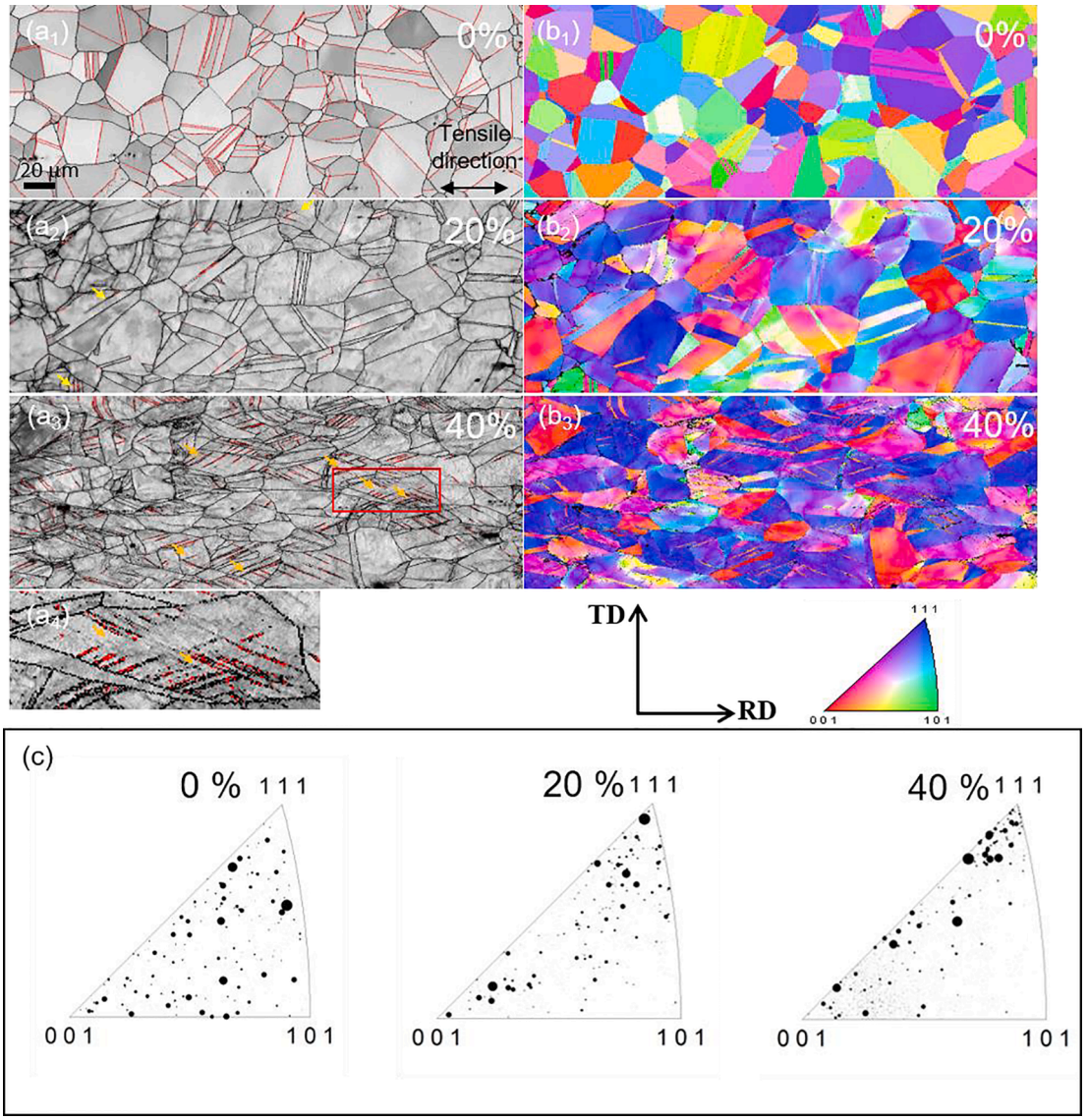

Fig. 2. EBSD (a) image quality (IQ), (b) rolling direction inverse pole figure (RD IPF) maps, and (c) RD IPF of the annealed material (a_1, b_1, c_1), and after 20% (a_2, b_2, c_2), and 40% strain (a_3, b_3, c_3). The black lines and the red lines indicate high angle grain boundaries and Σ3 twin boundaries, respectively. Thin deformation twins at 20% strain and double twinning system at 40% strain are indicated by yellow arrows and orange arrows, respectively. (a_4) zoom-in image obtained from the red box in (a_3), showing the development of the double twinning system. In IPFs, the sizes of the dots indicate relative grain sizes. The random grain orientation in the annealed material changes toward blue ⟨111⟩ and red ⟨100⟩ orientations // tensile direction. All the EBSD micrographs have the same scale bar as (a_1).

10%-strained, and the 20%-strained material (Fig. 3(a)) show a very small amount of the HCP phase and more at the fracture strain (~48% strain). The phase fraction was estimated from the integral intensities of corresponding peaks of the XRD pattern, referred to as the reference intensity ratio (RIR) method (Steve, 2000). The XRD pattern obtained from near the 223 K fracture surface show the overlapped FCC (111) and HCP (0002) peak at the 2θ range from 43 to 43.5 °, which is difficult to decompose because the peaks are too close. Thus, the HCP fraction near the fracture surface ranges from 20.6% when excluding the HCP (0002) peak to 29.1% when assuming that the overlapped peak entirely corresponds to the HCP (0002) peak. The EBSD RD IPF map near the fracture surface (Fig. 3 (b)) also shows dominant blue ⟨111⟩ and red ⟨100⟩ orientations // tensile direction, which is similar to the grain orientations of the material deformed at room temperature. The EBSD phase map of the fractured material (Fig. 3(c)) shows thick HCP plates and some blocky HCP domains, with the HCP volume percentage of 33%.

Table 2 compares tensile properties, i.e. YS, UTS, TE, and strain hardening capacity represented by UTS-YS, at various deformation temperatures reported for the CoCrFeMnNi HEA and $Fe_{40}Mn_{40}Co_{10}Cr_{10}$ HEA. All of the 77 K CoCrFeMnNi tensile properties, i.e. YS, UTS, TE, and UTS-YS, are superior to room temperature properties, which is attributed to additional activation (Otto et al., 2013) or earlier onset (Laplanche et al., 2016) of deformation twinning during cryogenic deformation. At 298 K, the $Fe_{40}Mn_{40}Co_{10}Cr_{10}$ HEA mainly exhibits deformation twinning, and at lower temperatures, deformation-induced HCP transformation occurs, consistent with the present work. The joint activation of deformation twinning and deformation-induced HCP phase was reported for the 8 μm fine-grained material deformed at 77 K (He et al., 2019) and for the 150–180 μm coarse-grained material deformed at 298 K(Chandan et al., 2019).

The transition temperature of the $Fe_{40}Mn_{40}Co_{10}Cr_{10}$ alloy at which deformation mechanisms change from deformation twinning to deformation-induced HCP transformation is considerably higher than other HEAs deformed by dislocation slip and deformation twinning at room temperature (Huo et al., 2017; Laplanche et al., 2016). For example, the CoCrFeMnNi HEA deformed at 77 K mainly exhibited dislocation slip and deformation twinning without deformation-induced HCP transformation (Laplanche et al., 2016; Otto et al., 2013).

3.2. *Stacking fault energy of $Fe_{40}Mn_{40}Co_{10}Cr_{10}$ at room temperature*

To investigate the relationship between SFE and deformation mechanisms, the SFE was measured using weak-beam dark field imaging of dissociated dislocations [Steffens et al. 1987]. Fig. 4(a) shows a representative weak-beam dark-field image showing a

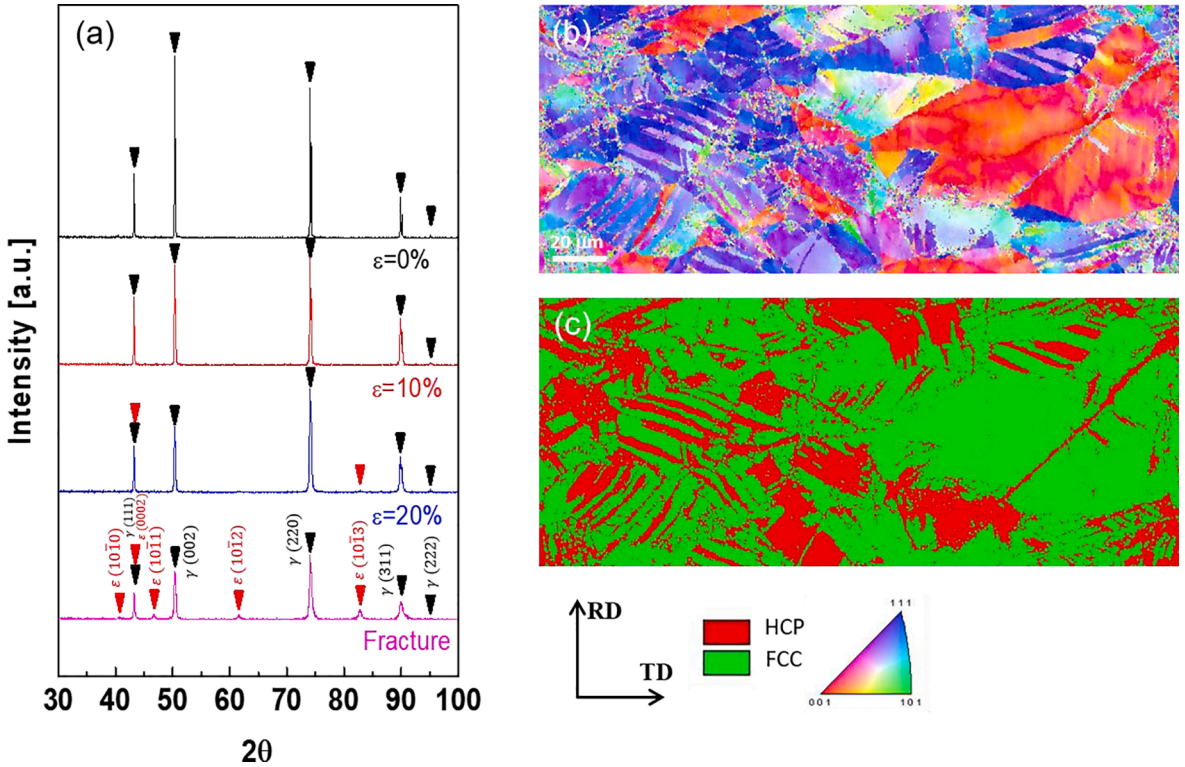

Fig. 3. XRD patterns and EBSD micrographs of the material deformed at 223 K. (a) XRD patterns of the as-annealed, 10% strained, 20% strained material show negligible HCP peaks, but a higher intensity of HCP peaks near the fracture surface (~48% strain). (b) The RD inverse pole figure (IPF) map near the fracture surface shows dominant blue ⟨111⟩ and red ⟨100⟩ orientations // tensile direction. (c) Phase map from the same scan area near the fracture surface shows thick HCP plates and some blocky HCP domains, with the HCP volume percentage of 33%. (b) and (c) have the same scale bar.

Table. 2
Comparison of tensile properties, i.e. YS, UTS, TE, and strain hardening capacity represented by UTS-YS, at various deformation temperatures reported for the CoCrFeMnNi HEA and $Fe_{40}Mn_{40}Co_{10}Cr_{10}$ HEA.

Material	Temperature [K]	Grain size [μm]	YS [MPa]	UTS [MPa]	TE [%]	UTS-YS [MPa]	Deformation mechanisms	Reference
CoCrFeMnNi	298	4.4	360	660	51	300	Dislocation slip	Otto et al. (2013)
	298	50	190	570	60	380		
	298	155	170	530	57	360		
	298	17	265	600	48	335	Dislocation slip, Deformation twinning	Laplanche et al. (2016)
	77	4.4	565	1100	70	535	Dislocation slip, Deformation twinning	Otto et al. (2013)
	77	50	385	980	90	595		
	77	155	350	910	84	560		
	77	17	460	1060	60	600	Dislocation slip, Deformation twinning	Laplanche et al. (2016)
$Fe_{40}Mn_{40}Co_{10}Cr_{10}$	298	109	240	489	58	249	Dislocation slip, Deformation twinning	Deng et al. (2015)
	298	8	272	481	47	209	Dislocation slip, Deformation twinning	He et al. (2019)
	298	150–180	240	514	47	274	Dislocation slip, Deformation twinning, Deformation-induced HCP transformation	Chandan et al. (2019)
	298	20	208	475	55	267	Dislocation slip, Deformation twinning	This work
	298	130	243	554	42	311	Dislocation slip, Deformation twinning	Chandan et al. (2021)
	223	20	246	583	48	337	Dislocation slip, Deformation-induced HCP transformation	This work
	173	130	421	803	80	382	Dislocation slip, Deformation twinning, Deformation-induced HCP transformation	Chandan et al. (2021)
	77	8	567	1003	65	436	Dislocation slip, Deformation twinning, Deformation-induced HCP transformation	He et al. (2019)

dissociated dislocation in the 298 K 2% strained material. The perfect dislocation decomposes into the two partial dislocations at the constriction indicated by the yellow arrow, where the following dislocation reaction occurs:

$$\frac{a}{2}\left[1\bar{1}0\right] \rightarrow \frac{a}{6}\left[1\bar{2}1\right] + \frac{a}{6}\left[2\bar{1}\bar{1}\right] \quad (1)$$

The partial dislocation separation was directly measured from the image of dissociated dislocations. The measurement examples are presented in Fig. 4(a), i.e. 7.7, 11.7, and 10.4 nm. At the locations where the partial dislocation separation was measured, the angle between the Burgers vector of the perfect dislocation and the dislocation line, θ, was also measured. Among the three {220} diffraction conditions available in the ⟨111⟩ zone axis of an FCC crystal structure, only one {220} diffraction vector renders both partial

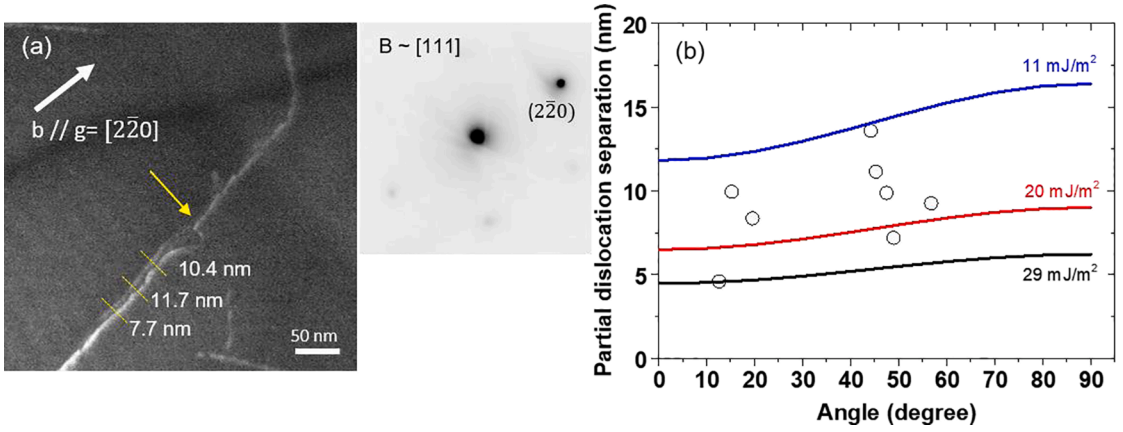

Fig. 4. Measurement of SFE using the TEM partial dislocation separation method using (a) a weak-beam dark field image and the corresponding diffraction pattern showing a dissociated dislocation in the 298 K 2% strained material. Both the diffraction vector (g) and the Burgers vector of the perfect dislocation (b) are parallel to the [2$\bar{2}$0]. The yellow arrow indicates constriction, where two Shockley partial dislocations combine into a perfect dislocation. (b) Comparison of the true partial dislocation separation derived from the experimental measurements and the theoretically predicted curves of the SFE using Eq. (2), which yields the SFE value of 20±9 mJ/m^2. The two outer curves indicate an estimated maximum error so that all the data points are within the two curves. The curve in the middle represents a curve with the average SFE value.

dislocations visible. In the two-beam condition for $g=(2\bar{2}0)$ (the DP in Fig. 4(a)), the Burgers vector of the perfect dislocation (b) is parallel to the diffraction vector (g) since both partial dislocations are visible. From the measurements of several dissociated dislocations, the observed partial dislocation separation, d_{obs}, ranges from 7.7 nm to 15 nm while the angle between the Burgers vector of the perfect dislocation and the dislocation line, θ, ranges from 12.7° to 56.8° The true partial dislocation separation was obtained from the measured partial dislocation separation considering the dislocation core effect on the partial dislocation separation (Williams and Carter, 1996). The SFE was estimated using the following equation (Aerts et al., 1962):

$$d = \frac{G|b_p|^2}{8\pi\gamma} \cdot \frac{2-\upsilon}{1-\upsilon}\left(1 - \frac{2\nu\cos 2\theta}{2-\upsilon}\right) \quad (2)$$

d and γ represents true partial separation and SFE, respectively. G is the shear modulus of the $Fe_{40}Mn_{40}Co_{10}Cr_{10}$ HEA (76 GPa) (Picak et al., 2019), b_p is the magnitude of the Burgers vector of the partial dislocations (0.148 nm), calculated using the lattice parameter of the $Fe_{40}Mn_{40}Co_{10}Cr_{10}$ HEA (0.3621 nm) (Deng et al., 2015) and υ is the Poisson's ratio of the FeNiCoCrMn alloy (0.26) (Wu et al., 2019). The comparison of the true partial dislocation separation derived from the experimental measurements and Eq. (2) yields the SFE value of 20±9 mJ/m^2 (Fig. 4(b)). Table 3 compares room temperature SFE values reported for the CoCrFeMnNi HEA and $Fe_{40}Mn_{40}Co_{10}Cr_{10}$ HEA.

3.3. Deformation mechanisms of $Fe_{40}Mn_{40}Co_{10}Cr_{10}$ at room temperature

TEM BF images of the room temperature 2% strained material, obtained from various two-beam conditions are shown in Fig. 5. The matrix shows a low dislocation density with a higher density of dislocations near the grain boundary indicated by the red arrows. The TEM image obtained from the two-beam condition with $g=(2\bar{2}0)$ (Fig. 5(b)) shows overlapped contrast of two dislocations as indicated by the yellow arrows. The two-beam condition with $g=(002)$ (Fig. 5(d)) exhibits stacking fault fringes. The diffraction contrast analysis indicates that the observed dislocations are extended dislocations consisting of two Shockley partial dislocations with the fringe contrast (white arrows in Fig. 5(d)) corresponding to a stacking fault present in-between the two dislocations. The low SFE of the investigated material, i.e. 20±9 mJ/m^2, could lead to easy dissociation of perfect dislocation into Shockley partial dislocations.

TEM images of another region of the 2% strained material are shown in Fig. 6. In Fig. 6(a), the dislocations are mostly aligned along the $(1\bar{1}1)$ plane trace and the $(\bar{1}11)$ plane trace, which indicates the occurrence of multiple slip. In contrast to the image in Fig. 5, stacking fault contrast is not present, indicating that the dislocations are perfect dislocations. Thus, the dislocation pattern observed in the region corresponds to the Taylor lattice structure of perfect dislocations. The Taylor lattice consists of dislocations parallel to the one or more highly stressed glide plane, and its boundaries block the dislocation motion (Kuhlmann-Wilsdorf, 1989). In another grain (Fig. 6(b)), the upper region enclosed by the orange lines shows dislocations mostly aligned along the $(\bar{1}11)$ plane trace. Note that the faint contrast is present along the $(1\bar{1}1)$ plane trace, indicating that dislocations are also present on the $(1\bar{1}1)$ plane, but they are out of contrast by the $g \bullet b = 0$ criterion. The representative dislocations present on the $(1\bar{1}1)$ plane and the $(\bar{1}11)$ plane are indicated by the white arrows and the yellow arrows, respecptively. Some dislocations in the upper region, indicated by the red arrows, show clear contrast of extended dislocations. The lower region shows a complex arrangement of dislocations from multiple planes, i.e. the two edge-on planes and inclined planes. Some dislocations in the lower region also show a contrast of extended dislocations indicated by the red arrows. The dislocation pattern observed in the region corresponds to the Taylor lattice structure consisting of extended dislocations or perfect dislocations.

TEM BF images of the 5% strained material are shown in Fig. 7. The grain with an annealing twin shows a high density of dislocations in-between the annealing twin boundary and the grain boundary (Fig. 7(a)). Annealing twin boundaries were reported to act as barriers for dislocation motion in the CoCrNi medium entropy alloy (Schneider et al., 2020). Fig. 7(b_1) presents a grain showing extended dislocations on different slip planes. Fig. 7(b_2) presents the region with the same grain as Fig. 7(b_1) and shows that a Lomer-Cottrell lock formed from interactions of two Shockley partial dislocations is present parallel to the $[1\bar{1}0]$ crystallographic direction. The observed Lomer-Cottrell lock is similar to diffraction contrast, parallel to the ⟨110⟩ crystallographic direction, observed in the Fe-30.5Mn-2.1Al-1.2C (wt.%) TWIP steel (Gutierrez-Urrutia and Raabe, 2012) and the $Al_{0.1}$CoCrFeNi (at.%) HEA (Xu et al., 2018). The Lomer-Cottrell locks act as barrier for dislocation motion and result in the work hardening of materials (Xu et al., 2018).

Table. 3
Comparison of room temperature SFE values reported for the CoCrFeMnNi HEA and $Fe_{40}Mn_{40}Co_{10}Cr_{10}$ HEA.

Material	SFE (mJ/m2)	Method	Reference
CoCrFeMnNi	25.5–27.3	Density functional theory: VASP (Vienna ab initio simulation package)	(Zaddach et al., 2013)
	18.3–19.6	Density functional theory: Exact muffin-tin orbital (EMTO) method combined with the coherent potential approximation (CPA)	
	21	Density functional theory: Exact muffin-tin orbital (EMTO) method combined with the coherent potential approximation (CPA)	(Huang et al., 2015)
$Fe_{40}Mn_{40}Co_{10}Cr_{10}$	13±4	TEM: Dislocation node method	(Picak et al., 2019)
	20±9	TEM: Partial dislocation separation method	This work

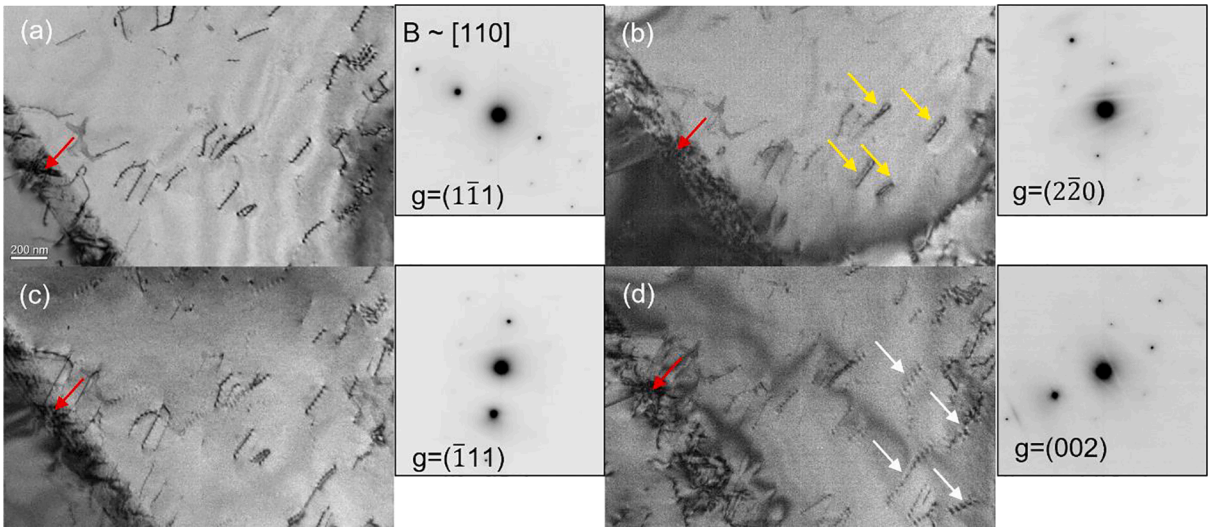

Fig. 5. TEM analysis of the extended dislocations using various two-beam diffraction conditions for the room temperature 2% strained material. The red arrows indicate the grain boundary. The overlapped contrast of two dislocations (yellow arrows in (b)) and stacking fault fringes (white arrows in (d)) indicate characteristics of extended dislocations. All the TEM micrographs have the same scale bar as (a).

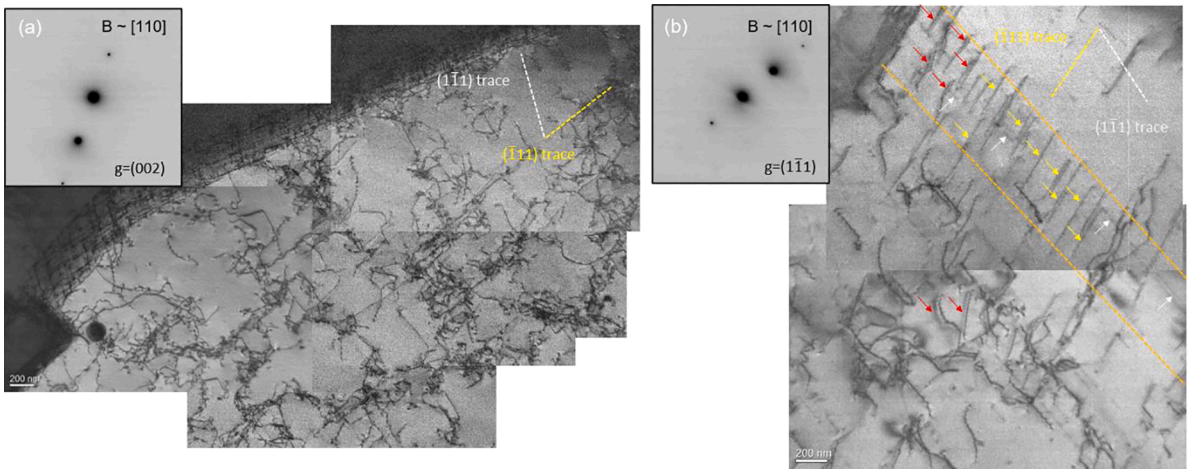

Fig. 6. TEM images of the room temperature 2% strained material showing (a) the Taylor lattice structure of perfect dislocations and (b) the Taylor lattice structure consisting of extended dislocations or perfect dislocations. The (1$\bar{1}$1) plane trace and the ($\bar{1}$11) plane trace are indicated by the white dashed line and the yellow dashed line, respectively. In (b), the upper region enclosed by the orange lines shows that most dislocations are present on the (1$\bar{1}$1) plane and the ($\bar{1}$11) plane. The representative dislocations present on the (1$\bar{1}$1) plane and the ($\bar{1}$11) plane are indicated by the white arrows and the yellow arrows, respectively. The lower region shows a complex arrangement of dislocations from multiple planes. Extended dislocations are indicated by the red arrows.

The heterogeneous dislocation patterns observed in the same grain are provided in Fig. 7(c) and (d). The two distinct features are observed near the grain boundary (Fig. 7(c)), i.e. the region showing a high dislocation density, indicated by the white arrows, and the region showing a low dislocation density, indicated by the yellow arrows. The region showing a low dislocation density could correspond to the initial stage of dislocation cell structure. In the grain interior (Fig. 7(d)), the dislocation density is relatively low and the contrast of dislocation loops is present as indicated by the yellow arrow. The formation of dislocation loops were reported to be promoted by high cross slip activity (Jiang et al., 2019).

TEM BF images of the 10% strained material are provided in Fig. 8, showing a higher dislocation density than the microstructure of the 5% strained material. The TEM images in Fig. 8(a)-(d) were obtained from the same grain and show heterogeneous dislocation patterns in different locations of the same grain. Fig. 8(a) shows that most dislocations are present on (1$\bar{1}$1) and ($\bar{1}$11) planes, which are characteristics of planar slip. The dislocations are not extended dislocations, and they are probably perfect dislocations. The observed dislocation pattern is consistent with the Taylor lattice structure. In some regions, the dislocation density is high, which corresponds to the HDDW structure. In Fig. 8(a) and (b), the yellow dashed line and the white dashed line indicate the ($\bar{1}$11) plane trace and the (1$\bar{1}$1)

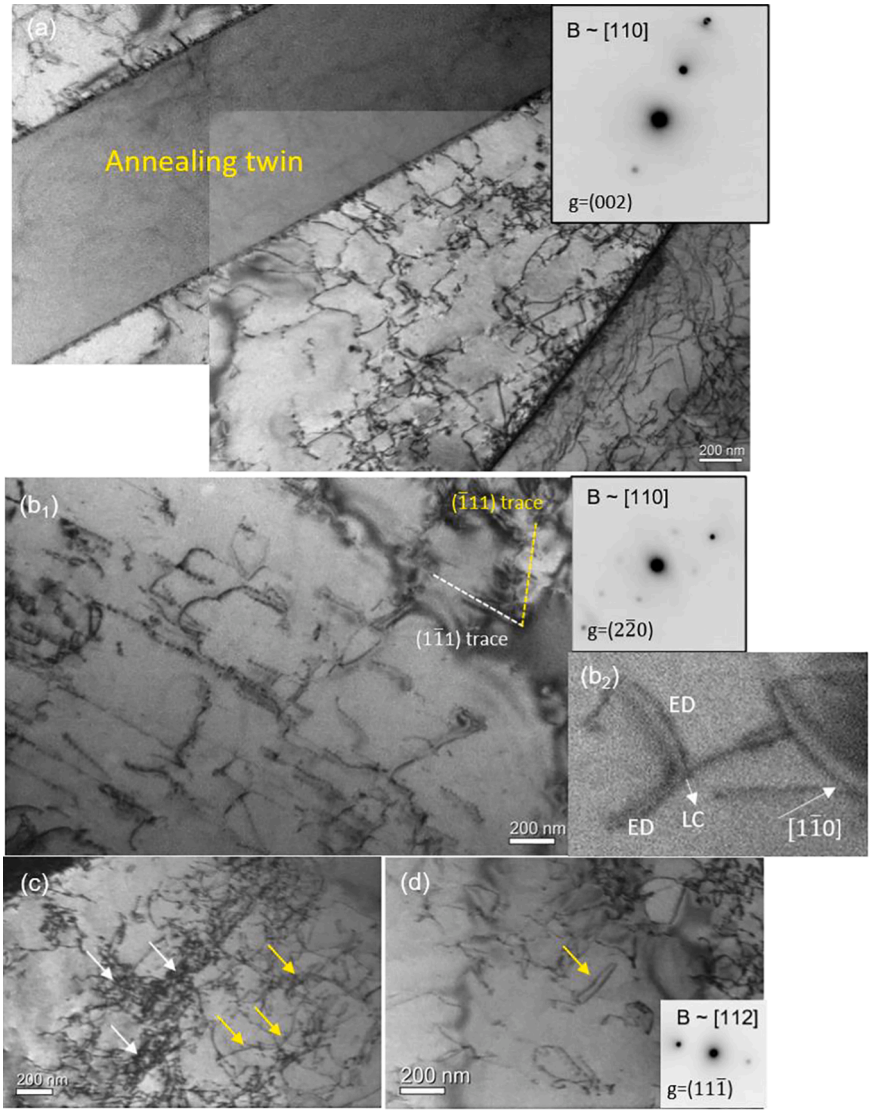

Fig. 7. TEM images of the room temperature 5% strained material. (a) A high density of dislocations is present in-between the annealing twin boundary and the grain boundary. (b_1) Extended dislocations are present on different slip planes. The $(1\bar{1}1)$ plane trace and the $(\bar{1}11)$ plane trace are indicated by the white dashed line and the yellow dashed line, respectively. (b_2) The region with the same grain as (b_1) shows that a Lomer-Cottrell lock formed from interactions of two Shockley partial dislocations is present parallel to the $[1\bar{1}0]$ crystallographic direction. ED and LC denote extended dislocations and a Lomer-Cottrell lock, respectively. (c, d) heterogeneous dislocation patterns observed in the same grain. (c) The region near the grain boundary consists of the region showing a high dislocation density, indicated by the white arrows, and the region showing a low dislocation density, indicated by the yellow arrows. (d) The region in the grain interior shows a low dislocation density and a dislocation loop indicated by the yellow arrow.

plane trace, respectively The dislocations in Fig. 8(a) are mostly aligned with the two plane traces while the dislocations in Fig. 8(b) are present on $(\bar{1}11)$ planes, but not on the $(1\bar{1}1)$ planes, indicating their deviation from the $(1\bar{1}1)$ plane. The dislocation pattern has a similar characteristic with dislocation cell block structure consisting of the dislocation wall areas showing high dislocation density and the almost dislocation-free areas inside the dislocation walls. The cell block structures are delimited by HDDWs (Gutierrez-Urrutia and Raabe, 2012). The dislocation patterns observed in Fig. 8(c) and (d) are similar to that observed in Fig. 8(b). The dislocation cell block size in Fig. 8(c) is approximately 600 nm and that in Fig. 8(d) is larger than 1 μm, which indicates inhomogeneous cell block size even in a single grain.

In another grain of the 10% strained material, two inclined elongated stacking faults emitted from the grain boundary are observed (Fig. 8(e)). The partial dislocation contrast inside the stacking faults (yellow arrows) indicates that the faults are overlapped. A moderate density of dislocations is observed near the stacking faults. It should be noted that deformation twins were not identified in the TEM characterization, indicating the absence or very low volume fraction of deformation twins in the 10% strained material.

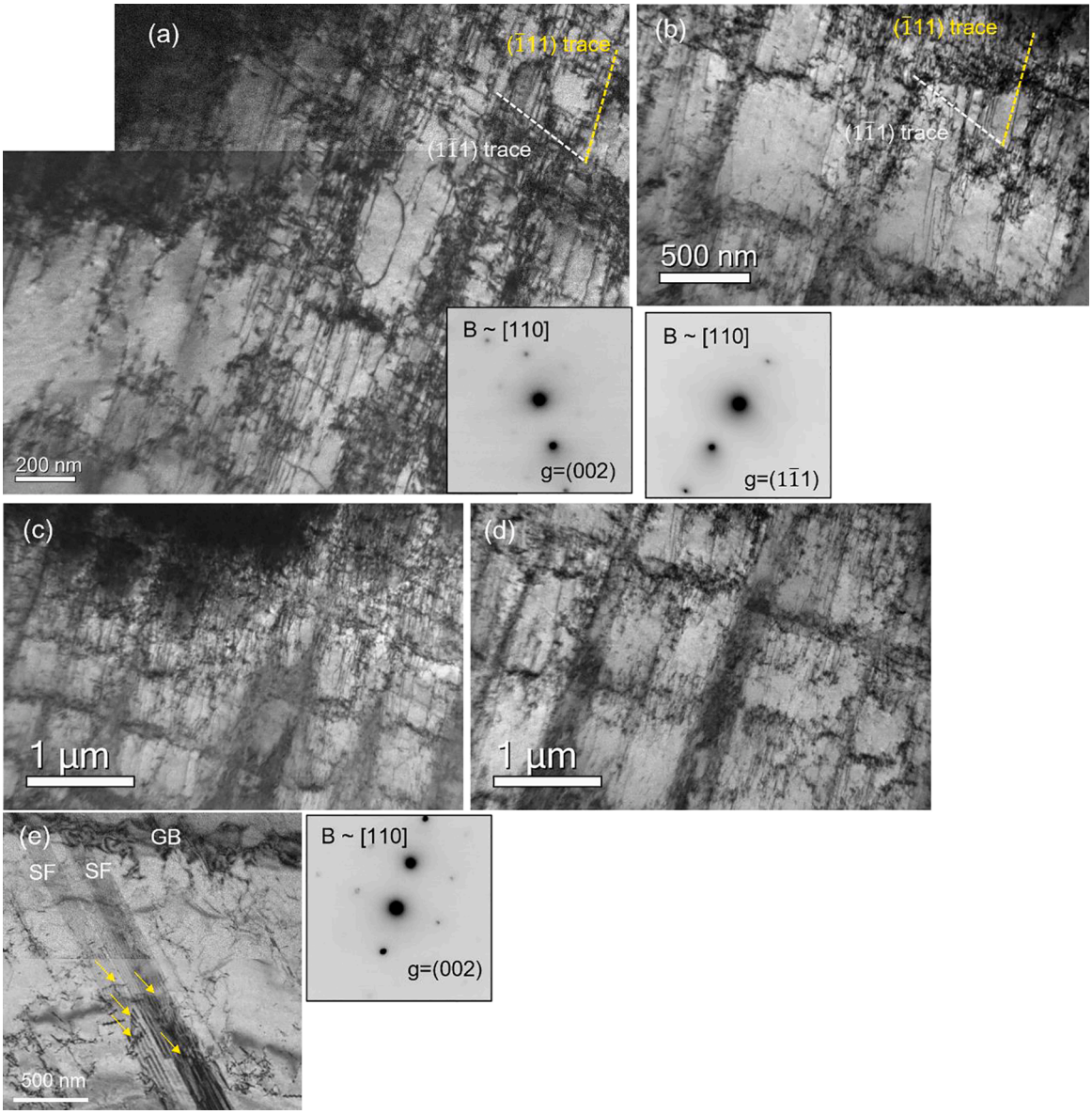

Fig. 8. TEM images of the room temperature 10% strained material. The images in (a)-(d) are from the same grain. (a) The Taylor lattice structure and the HDDW structure. Most dislocations are present on $(1\bar{1}1)$ and $(\bar{1}11)$ planes, indicated by the white dashed line and the yellow dashed line, respectively. (b) Dislocation cell block structure. The dislocations are present on $(\bar{1}11)$ planes, but not on the $(1\bar{1}1)$ planes, indicating their deviation from the $(1\bar{1}1)$ plane. (c, d) inhomogeneous cell block size with 600 nm for (c) and larger than 1 μm for (d). (e) Two inclined elongated stacking faults emitted from the grain boundary. The grain boundary and stacking faults are denoted by GB and SF, respectively. The partial dislocation contrast inside the stacking faults (yellow arrows) indicates that the faults are overlapped.

However, the elongated stacking faults can be regarded as a precursor of deformation twins (Kim et al., 2017).

TEM images of the 20% strained material are provided in Fig. 9. Fig. 9(a) presents a grain showing deformation twin bands. Fig. 9 (b) shows coexistence of the diffraction spots from the FCC matrix (orange lines) and the deformation twins (red lines). The twinning plane is $(1\bar{1}1)$ and the thickness of the deformation twin bands is approximately 100 nm. A high density of dislocations is present near the deformation twins. The observed dislocation pattern is similar to the dislocation cell structure. High-resolution TEM analysis in Fig. 9(c) shows a stacking fault inside the matrix and a deformation twin. Mirrored stacking sequence of the matrix and twin is observed across the twin boundary. The twin boundary seems to be highly distorted due to a high level of local deformation. Fig. 9(d) shows a twin-free grain showing dislocation cell structure. Some of the dislocation cell structure seems to be elongated. An inclined deformation twin showing fringe contrast (white arrow) is shown in Fig. 9(e). The dense dislocation structures are mainly present along the $(1\bar{1}1)$ plane of the matrix, which corresponds to the HDDW structure. The deformation twin connected to the grain boundary

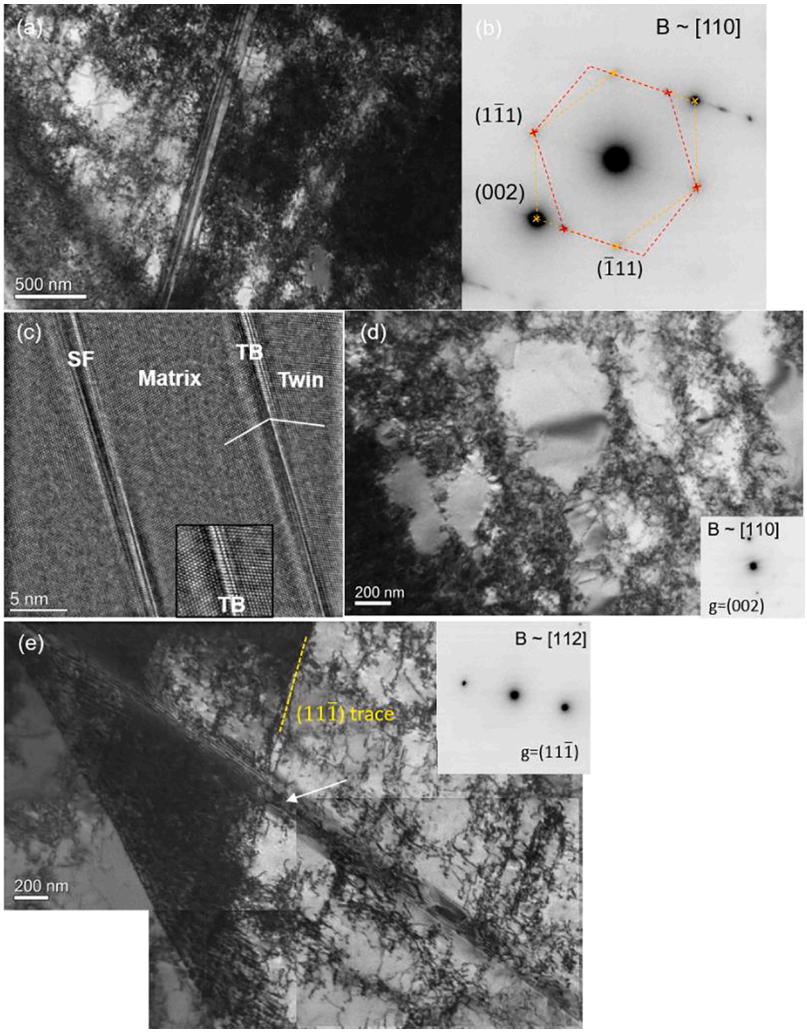

Fig. 9. TEM images of the room temperature 20% strained material. (a) Deformation twin bands and dislocations. (b) DP obtained from the BF image in (a), showing coexistence of the diffraction spots from the FCC matrix (orange lines) and the deformation twins (red lines). (c) High-resolution TEM image showing a stacking fault inside the matrix and a deformation twin. Mirrored stacking sequence of the matrix and twin is observed across the twin boundary. SF denotes a stacking fault and TB denotes a twin boundary. The inset shows magnified HRTEM image near the TB. (d) A twin-free grain showing dislocation cell structure. (e) An inclined deformation twin showing fringe contrast (white arrow) and the HDDW structure on the (1$\bar{1}$1) plane.

shows the dislocation contrast inside the twin, related to twinning partial dislocations and a part of HDDW simultaneously imaged through the TEM foil. The inclined character of the deformation twins interferes with description of dislocation interactions at the twin boundary.

TEM BF images of the 40% strained material are provided in Fig. 10. Fig. 10(a) shows parallel deformation twins. The thickness of the deformation twins is approximately 36 nm. Dislocation cell structures are present near the deformation twins. In another region of the same grain, the primary twins and the secondary twins are visible (Fig. 10(b)). The thickness of the primary twins is approximately 39 nm while that of the secondary twin is approximately 25 nm. The fine thickness of the secondary twins is related to the fact that deformation twins generally thicken as deformation proceeds. The observed deformation twins in Fig. 10(b) are in the edge-on condition, indicating the dislocations present in-between primary twins and secondary twins are matrix dislocations. This suggests that the twin boundaries could interfere with motion of the matrix dislocations, referred to as the dynamic Hall-Petch effect (Bouaziz et al., 2008). In twin-free grains (Fig. 10(c) and (d)), dislocation cell structures with heterogeneous cell sizes are observed.

3.4. *Deformation mechanisms of $Fe_{40}Mn_{40}Co_{10}Cr_{10}$ at 223 K*

Fig. 11 shows TEM BF images of the 10% strained material at 223 K. The inhomogeneous dislocation pattern, i.e. HDDW structures parallel to the (1$\bar{1}$1) plane near the grain boundary and dislocation cell structures in the grain interior, is shown in Fig. 11(a).

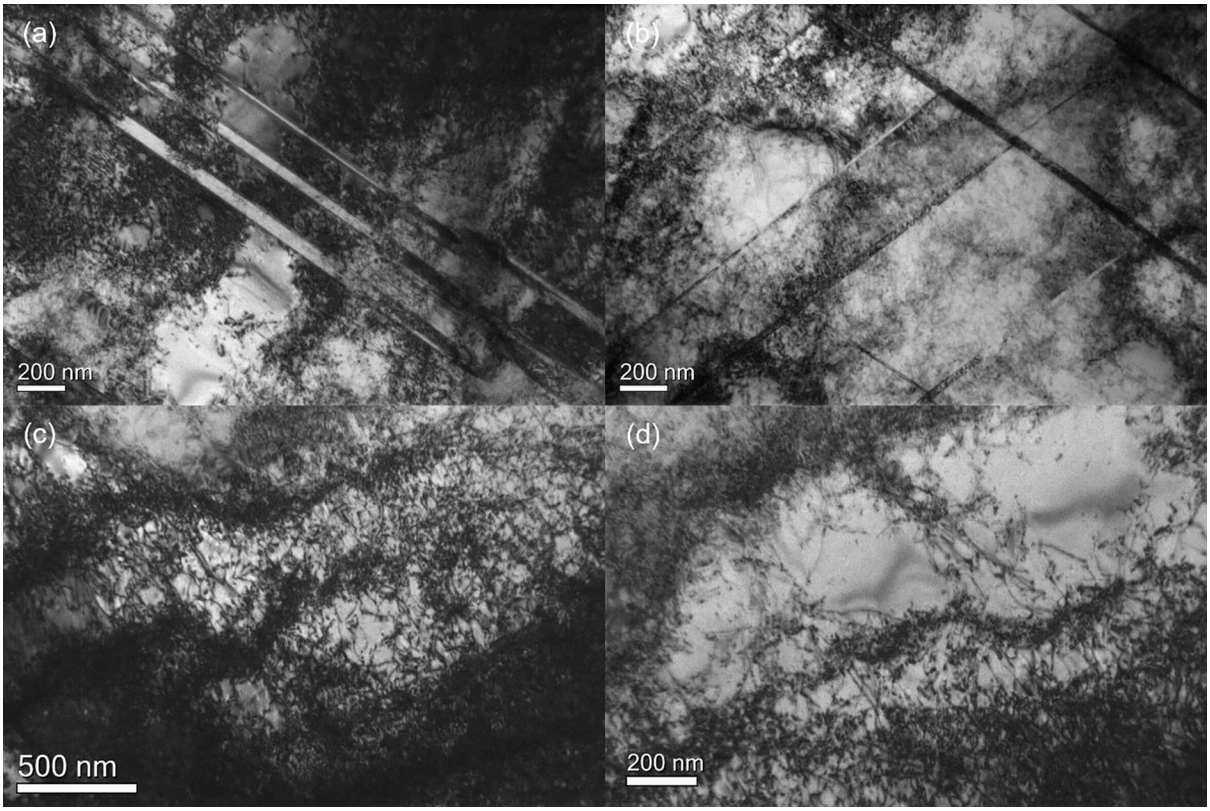

Fig. 10. TEM images of the room temperature 40% strained material. (a) Parallel deformation twins with dislocation cell structures near the deformation twins. (b) The primary twins and the secondary twins. A high density of matrix dislocations suggests that twin boundaries interfere with motion of matrix dislocations. (c, d) Dislocation cell structures with heterogeneous cell size.

Compared to the grain in Fig. 11(a), the grain in Fig. 11(b_1) shows much lower dislocation density, which enables individual dislocations to be identified. Some dislocations are present along the $(11\bar{1})$ plane, and the interaction between extended dislocations and the dislocations along the $(11\bar{1})$ plane is visible. Some dislocation loops are also visible as indicated by the white arrows. Fig. 11(b_2) presents the region with the same grain as Fig. 11(b_1) and shows that a Lomer-Cottrell lock formed from interactions of two Shockley partial dislocations is present parallel to the $[1\bar{1}0]$ crystallographic direction. Fig. 11(c) shows approximately parallel dense dislocation structures present across the entire grain. The dislocation density inside the dislocation structures is extremely high, and the slip plane of the dislocations could not be identified. The structures are expected to be the HDDW structures present on inclined {111} plane or non-crystallographic HDDW structures (Winther et al., 1997). It should be noted that a plate-type defect was observed in another grain, which is expected to be the HCP phase formed upon deformation (not shown here, but evident at larger strain in Fig. 12). However, the formation of the HCP phase is a minor contribution to the deformation at 10% strain. The initial stage of deformation up to the strain of 10% is mainly characterized by complex dislocation structures with inhomogeneous dislocation density.

TEM images of the 20% strained material are provided in Fig. 12 showing extensive deformation-induced HCP martensite. Fig. 12 (a) shows an inclined HCP plate and dislocations. The inclined plate could not be characterized by DPs due to its inclined character, but it is most likely deformation-induced HCP martensite. In the same grain, clear dislocation cell structures are present together with the plate-type defect. The grain in Fig. 12(b) shows HCP martensite plates parallel to the $(1\bar{1}1)$ plane of the FCC matrix with some dislocations. The average thickness of the HCP martensite plate is approximately 24 nm. The higher amount of dislocation contrast near the HCP martensite plates indicates their role as barrier for dislocation motion. The DF image and the DP in Fig. 12(c) provide clear evidence of the deformation-induced HCP martensite present in another grain. The average thickness of the HCP martensite plates is approximately 46 nm. The DP analysis shows that the $(1\bar{1}1)$ plane of the FCC matrix is parallel to the (0002) plane of the HCP plate. The BF images in Fig. 12(d) show that the observed HCP martensite plates in Fig. 12(c) are associated with the thick parallel HDDW structures. The HDDW structures are present across the entire grain and the length of the structures is approximately 14.4 μm. The characteristics of the HDDW structures are similar to those observed in Fig. 11(c). Since similar structures are already present in the 10%-strained material (Fig. 11(c)), the HDDW structures are expected to be formed prior to the formation of the HCP martensite plates.

The complex deformation microstructures of the material near the fracture surface are provided in Fig. 13. The high density of plate-type defects shown in Fig. 13(a) is a mixture of the FCC phase and the HCP phase. The red circles in Fig. 13(a) identify the areas where DPs were taken. Both of the DPs obtained from region (1) and region (2) exhibit a mixture of FCC and HCP phases. Comparison

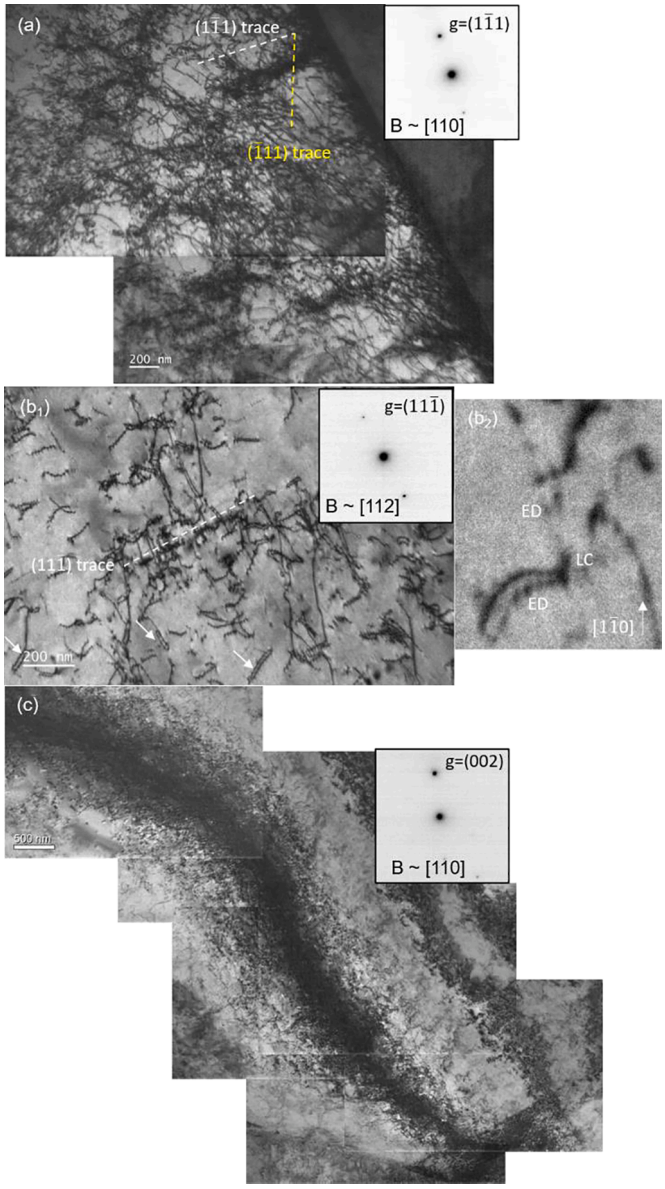

Fig. 11. TEM images of the 10% strained material at 223 K. (a) HDDW structures near the grain boundary and dislocation cell structures in the grain interior. The (1$\bar{1}$1) plane trace and the ($\bar{1}$11) plane trace are indicated by the white dashed line and the yellow dashed line, respectively. (b_1) Some dislocations are present along the (11$\bar{1}$) plane, and the interaction between extended dislocations and the dislocations along the (11$\bar{1}$) plane is visible. (b_2) The region with the same grain as (b_1). A Lomer-Cottrell lock formed from interactions of two Shockley partial dislocations is present parallel to the [1$\bar{1}$0] crystallographic direction. ED and LC denote extended dislocations and a Lomer-Cottrell lock, respectively. (c) Approximately parallel dense dislocation structures present across the entire grain, expected to be the HDDW structures present on inclined {111} plane or non-crystallographic HDDW structures.

of the DPs shows a rotation of the $(0002)_{HCP}$ // $(1\bar{1}1)_{FCC}$ plane by 12 ° The structure is similar to kink bands reported for plastically anisotropic materials (Barsoum et al., 2003; Churchman, 1955; Hagihara et al., 2016; Kim et al., 2015). Another region shows a completely HCP structure with a high density of defects. The three regions having band-like morphology show brighter contrast than the matrix. Some of the bands are several microns long. To characterize the bands, DP analysis was conducted. Region (1) only shows HCP diffraction spots and an extremely high density of planar defects are present parallel to the (0002) plane of the HCP matrix. Since the HCP structures are only formed by deformation, the planar defects most likely correspond to a very fine mixture of FCC, HCP plates, and stacking faults. Region (2) shows a mixture of HCP and FCC diffraction spots. Since the HCP diffraction spots originated from the matrix, the band is most likely FCC structure. Further, the {111} planes of the band are not associated with the (0002) plane of the HCP matrix, suggesting that the band was newly nucleated during deformation. The reverse transformation from deformation-induced HCP

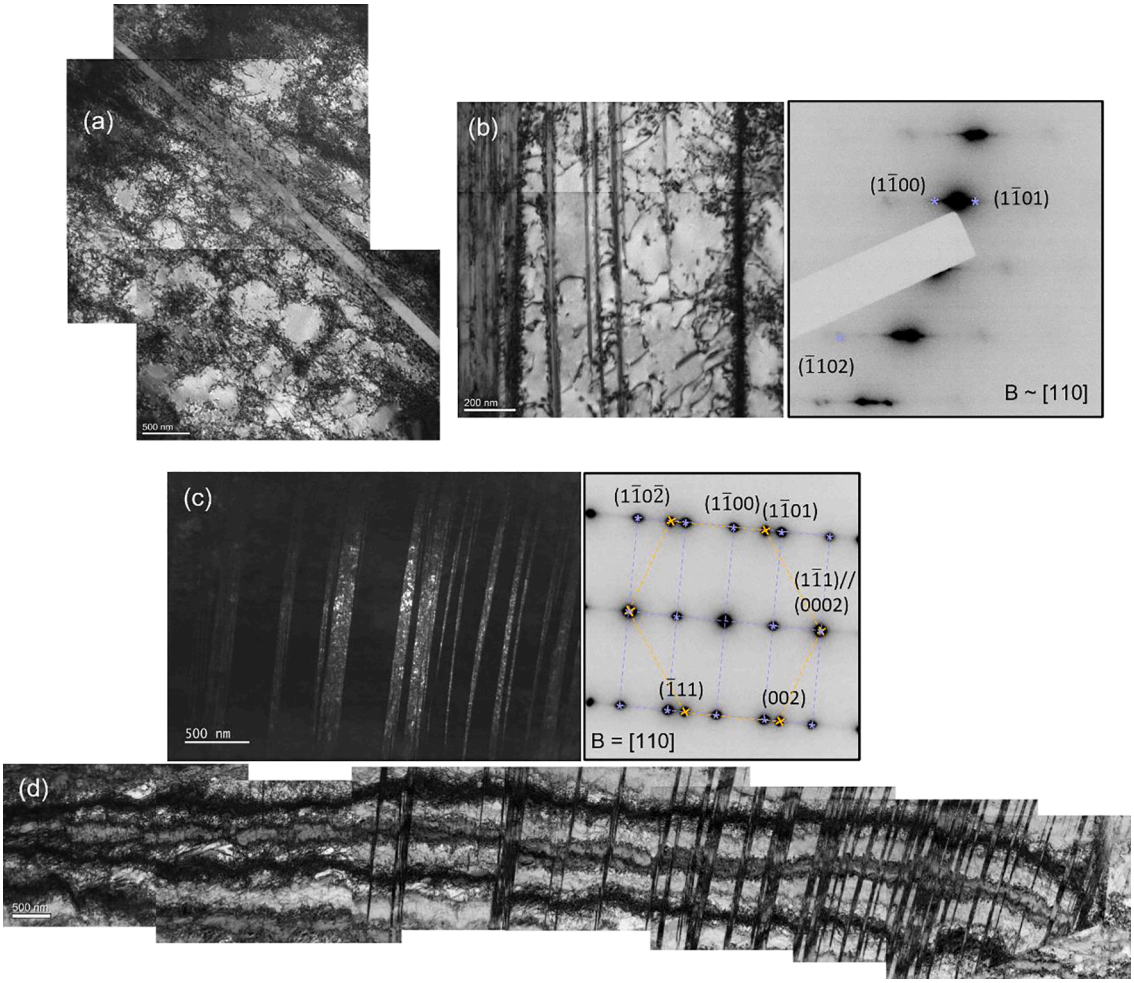

Fig. 12. TEM images of the 20% strained material at 223 K. (a) An inclined HCP plate and dislocation cell structure. (b) HCP martensite plates parallel to the (1$\bar{1}$1) plane of the FCC matrix with some dislocations. (c) A DF image showing the parallel deformation-induced HCP martensite. DP shows the coexistence of the diffraction spots from the FCC matrix (orange lines) and the HCP plates (light blue lines). The (1$\bar{1}$1) plane of the FCC matrix is parallel to the (0002) plane of the HCP plate. (d) Thick parallel HDDW structures present together with the deformation-induced HCP martensite.

phase to FCC phase has been reported in metastable HEA systems (Lu et al., 2018; Su et al., 2019; Wei et al., 2020). Su et al. (2019) reported the similar band-like FCC structures in the deformed HCP matrix of the 34% cold-rolled $Fe_{49.5}Mn_{30}Co_{10}Cr_{10}C_{0.5}$ (at.%) metastable HEA system and referred to the structure as micro shear bands. The grain shown in Fig. 13(d) shows the activation of multi-variant planar defects, most likely the HCP phase. The planar defects indicated by the yellow arrow are curved due to the severe deformation level. The curved HCP plate with its long axis aligned with the basal plane would lead to a rotation of the basal plane, which is similar to the kink bands shown in Fig. 13(a).

3.5. Summary of temperature-dependent deformation mechanisms of $Fe_{40}Mn_{40}Co_{10}Cr_{10}$

The observed deformation mechanisms of the investigated $Fe_{40}Mn_{40}Co_{10}Cr_{10}$ HEA at both room temperature and subzero temperature are illustrated in Fig. 14 and summarized in Table 4. The observed dislocation structures are almost identical for both deformation temperatures. The evolution of dislocation structures upon straining is similar to that observed for the Fe-30.5Mn-2.1Al-1.2C (wt.%) steel (Gutierrez-Urrutia and Raabe, 2012) and the $Fe_{40}Mn_{40}Co_{10}Cr_{10}$ HEA (Chandan et al., 2019).

4. Discussion

4.1. Effect of stacking fault energy on deformation mechanisms

With decreasing SFE in low SFE FCC materials, deformation mechanisms change from deformation twinning to deformation-

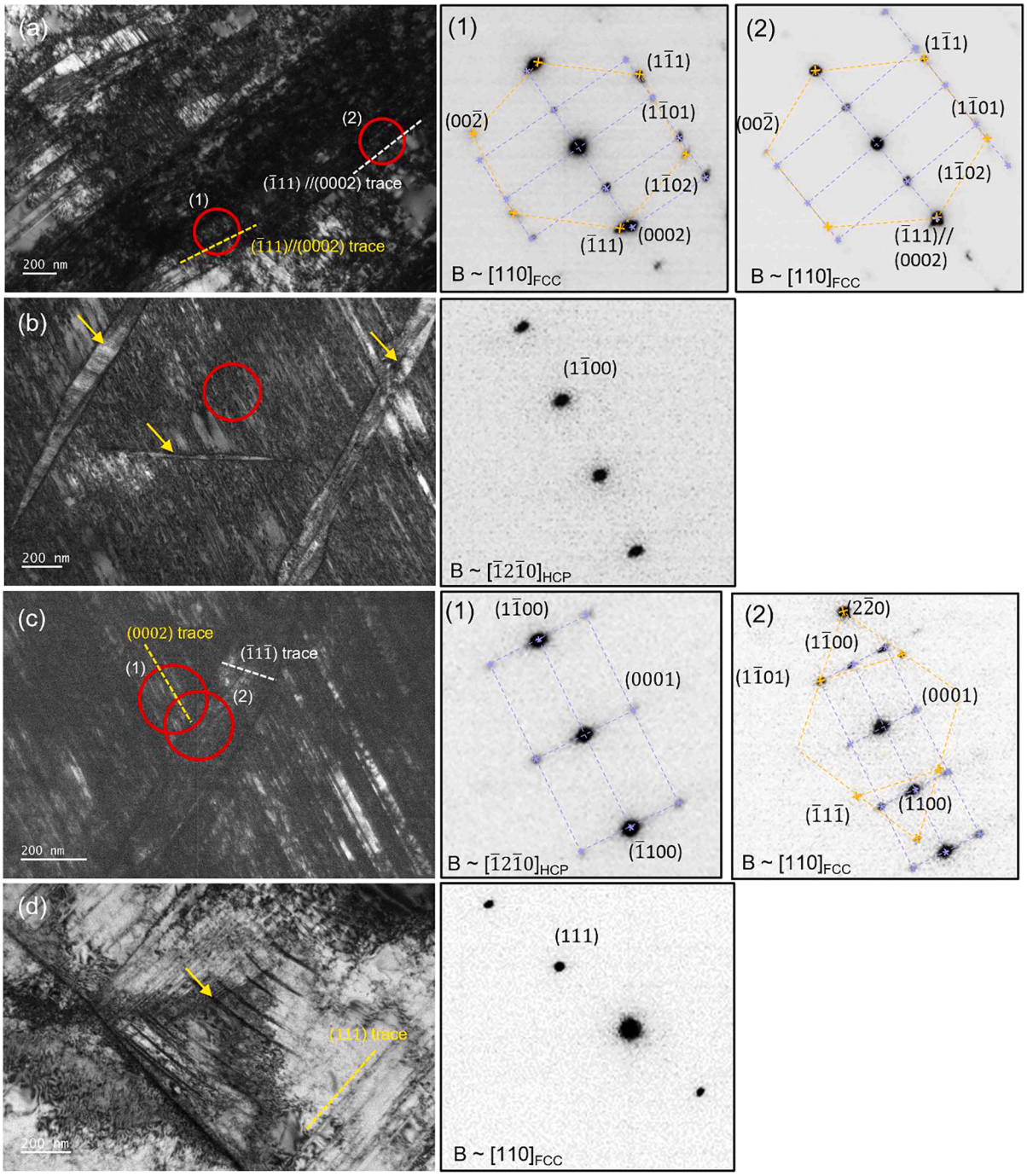

Fig. 13. TEM images of the fractured material at 223 K. (a) The kink band consisting of a mixture of the FCC phase and the HCP phase, with a rotation of the $(0002)_{HCP}$ // $(1\bar{1}1)_{FCC}$ plane by 12 ° (b) The area with the HCP phase having a high density of defects. The three regions having band-like morphology show brighter contrast than the matrix. (c) DP analysis showing that the band exhibits FCC structure, formed upon reverse transformation from deformation-induced HCP phase to FCC phase. (d) A grain showing the activation of multi-variant planar defects, most likely the HCP phase. The planar defects indicated by the yellow arrow are curved.

induced HCP martensitic transformation. A low SFE facilitates the formation of a wide stacking fault required for the nucleation of a deformation twin or deformation-induced HCP martensite. The $Fe_{40}Mn_{40}Co_{10}Cr_{10}$ alloy is reported to exhibit a positive temperature dependence of SFE (Huang et al., 2018), leading to a decrease of SFE as deformation temperature decreases from 298 K to 223 K. The decrease of SFE results in the observed transition from deformation twinning to deformation-induced HCP transformation as reported by He et al. (2019).

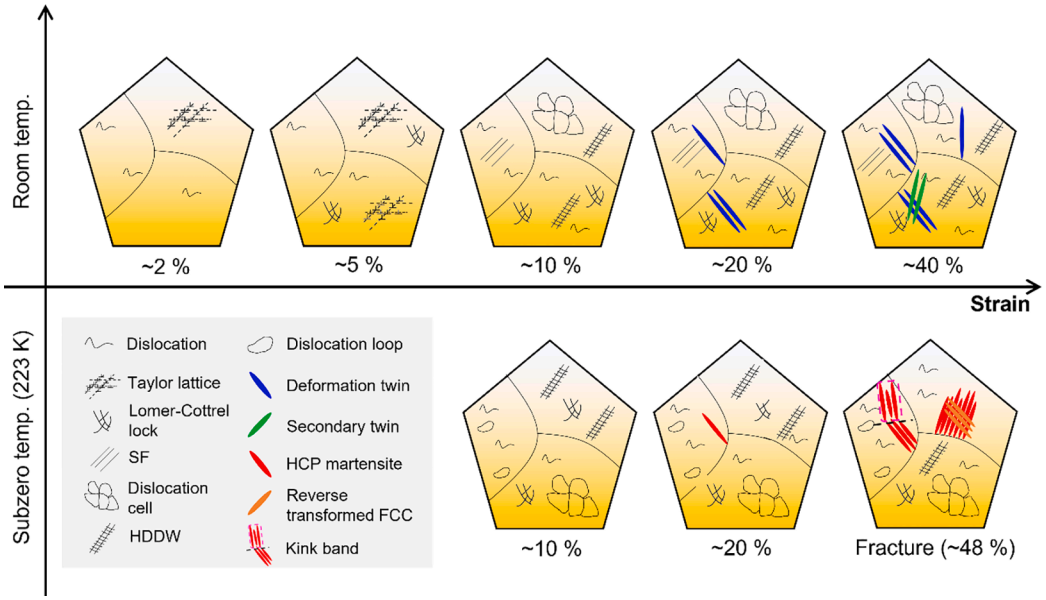

Fig. 14. Illustration showing deformation mechanisms of the investigated $Fe_{40}Mn_{40}Co_{10}Cr_{10}$ HEA at both room temperature and subzero temperature.

Table. 4
Summary of deformation mechanisms of the investigated $Fe_{40}Mn_{40}Co_{10}Cr_{10}$ HEA at both room temperature and subzero temperature.

RT	Strain	~10%	~20%	~40%
223 K	Phase	FCC		
	Deformation mechanisms	Dislocation slip	+ Deformation twins	+ Secondary twins
	Dislocation structures	Taylor lattice, Dislocation loop, Lomer-Cottrell lock, Dislocation cell, HDDW, SF		
		~10%	~20%	Fracture (~48%)
	Phase	FCC	FCC + HCP	
	Deformation mechanisms	Dislocation slip	+ Deformation-induced HCP phase	+ Kink banding of HCP phase, Reverse transformation from HCP to FCC
	Dislocation structures	Taylor lattice, Dislocation loop, Lomer-Cottrell lock, Dislocation cell, HDDW, SF		

The low SFE material is known to exhibit a large partial dislocation separation, leading to difficult cross slip and planarity of dislocation structures. Dislocation structures observed upon deformation at 223 K are quite similar to those observed for deformation at room temperature, i.e. HDDWs, dislocation cells, Lomer-Cottrell locks, and dislocation loops. This indicates that the decrease of SFE by decreasing deformation temperature (Allain et al., 2004; Huang et al., 2015; Olson and Cohen, 1976) would not highly influence the dislocation behavior of the investigated HEA. This is also consistent with the similar room temperature strain-dependent dislocation structures reported for the low SFE (~20 mJ/m^2) Fe-22Mn-0.6C (wt.%) steel (Gutierrez-Urrutia and Raabe, 2011), the $Fe_{40}Mn_{40}Co_{10}Cr_{10}$ HEA (Deng et al., 2015), and the high SFE (63 mJ/m^2) Fe-30.5Mn-2.1Al-1.2C (wt.%) steel (Gutierrez-Urrutia and Raabe, 2012).

Regarding the minor effect of SFE on dislocation structures, we hypothesize that (1) orientation effect could largely affect dislocation structures (Deng et al., 2015), and (2) large friction force originated from a large degree of dislocation/solute interaction in HEAs could resist motion of the Shockley partial dislocations (Shih et al., 2021), leading to the activation of perfect dislocations and easier cross-slip.

Landau et al. (2011) investigated strain-dependent dislocation structures of pure polycrystalline Al, Ni, and Au from room temperature up to 650 °C and suggested microstructural maps showing different dislocation patterns at various temperatures and strains. The materials showed universal strain-dependent dislocation structures having cell structures as the main mechanism. However, detailed previous works on strain-dependent dislocation structures at subzero temperatures and for low SFE materials are not available. Therefore, investigations on the temperature-dependent dislocation structures of various FCC materials, including subzero temperatures and low SFE materials, are essential to verify the universality of the present observations.

4.2. Evolution of dislocation structures

The initial stage of room temperature deformation is characterized by the activation of extended dislocations (Fig. 5). Because the

dislocation density is low, the extent of dislocation interactions is also low. The development of a Taylor lattice of perfect dislocations and interactions of extended dislocations are also observed at the same strain level, indicating strong dislocation interactions (Fig. 6). The development of the Lomer-Cottrell locks formed by interactions of extended dislocations on different slip planes could contribute to work hardening at the initial stage of deformation. However, the observed dislocation behavior is different from the dominant planar slip of perfect dislocations reported for the early stage of deformation of the CoCrFeMnNi alloy (Otto et al., 2013). We hypothesize that the presence of more various types of solute atoms in the CoCrFeMnNi alloy than in the $Fe_{40}Mn_{40}Co_{10}Cr_{10}$ alloy could cause more planarity of dislocations since solute atoms could affect the difficulty of cross slip by increasing the frictional stress of dislocations (Hong and Laird, 1990).

HDDWs, cell blocks, and cell structures are representative dislocation structures of FCC materials, which substantially influence deformation behavior. Fig. 8 provides evidence of simultaneous activation of HDDW and cell block structures in a single grain of the 10% deformed material. The microstructure provides evidence of inhomogeneous deformation in a single grain, i.e. activation of HDDW and cell block structures, and inhomogeneous cell block size. The transition from Taylor lattice to cell blocks and dislocation cells was reported for the high SFE Fe-30.5Mn-2.1Al-1.2C (wt.%) steel (Gutierrez-Urrutia and Raabe, 2012). A Taylor lattice is known to transform to cell structures as soon as more than one Burgers vector is available and glide on more than one plane is possible (Kuhlmann-Wilsdorf, 1989). Dislocation cell structures are also observed as seen in Fig. 9(d). At strains between 10% and 20%, the twin-free grains exhibit the development of various dislocation structures such as HDDWs, cell blocks, and cell structures. Because the dislocation structures are barriers for dislocation motion, this contributes to the hardening of the material. However, Gutierrez-Urrutia and Raabe (2011) suggested that they have smaller mechanical resistance than twin boundaries. HDDWs have been regarded as an impenetrable barrier for dislocation motion (Canadinc et al., 2005, 2007), and part of the blocked dislocations become trapped and add to the density of HDDWs. In contrast, dislocation cells have been regarded as weaker obstacles compared to HDDWs (Gutierrez-Urrutia and Raabe, 2011). The reported high mobility of cell walls could rule out the hypothesis that cell walls are strong barriers for dislocation motion (Kuhlmann-Wilsdorf, 1989).

4.3. Deformation twinning activated upon room temperature deformation

The measured SFE of the investigated cold-rolled and annealed $Fe_{40}Mn_{40}Co_{10}Cr_{10}$ (at.%) alloy is 20 ± 9 mJ/m^2 at room temperature (Fig. 4). The measured SFE value is in the SFE range of FCC materials (10–40 mJ/m^2) where deformation twinning can be activated (Kim and De Cooman, 2016; L. Remy, 1977; O. Grassel, 2000). The 40% deformed material shows profuse activity of deformation twinning as revealed by EBSD analysis (Fig. 2(a_3)). The microstructural characterization of the investigated material deformed at room temperature did not provide any evidence of deformation-induced HCP phase. The strain hardening rate curves in Fig. 1(b) show two characteristic stages, suggesting a change in the dominant deformation mechanisms at the transition from stage A to B. Specifically, stage A is characterized by dislocation-dominant deformation mechanisms and stage B is characterized by joint contribution of deformation twins and dislocations for the room temperature deformation. The stage B of the 223 K deformation is characterized by joint contribution of deformation-induced HCP phase and dislocations.

The isolated stacking faults (Fig. 9) are considered as a precursor of deformation twinning. As deformation proceeds, the single twinning system (Fig. 10, 20% strained material) could develop into the double twinning system (Fig. 11, 40% strained material). In low SFE FCC materials exhibiting deformation twinning, a grain with primary twins could nucleate secondary twins, usually at later stages of deformation (Asgari et al., 1997). The secondary twins intersect primary twins and further reduce the mean free path of dislocations, thus impeding slip on all slip systems and promoting high work hardening rates (Asgari et al., 1997). To elucidate the effect of deformation twinning on strain hardening behavior of the material, the following critical twinning stress for twin formation assuming a three-layer twin model was calculated (Steinmetz et al., 2013):

$$\tau_c = \frac{\gamma_{SFE}}{3b_p} + \frac{3Gb_p}{L_0} \tag{3}$$

Here, γ_{SFE} represents SFE of the material (20 mJ/m^2) as measured by the present work, b_p is the magnitude of the Burgers vector of the partial dislocations (0.148 nm). L_0 represents the distance between pinning points of a twin nucleus, the three partial dislocations. Here, 261 nm reported for a high Mn TWIP steel was used (Steinmetz et al., 2013). The calculated twinning shear stress is approximately 174 MPa, and the converted twinning stress using the Taylor factor of 3.06 is 533 MPa. This estimated twinning stress corresponds to the flow stress at the true strain of 0.175. The strain level is consistent with the transition point from stage A to stage B (Fig. 1(b)). From this theoretical and microstructural analysis, the transition point most likely corresponds to the initiation of deformation twinning. The TEM analysis for the 20% strained material shows a small amount of deformation twins. The interactions between deformation twins and dislocations and the development of a double twinning system could contribute to the sustained strain hardening of the material at the later stage of deformation at room temperature.

The thickness and internal structures of deformation twins could affect the strain hardening behavior of FCC materials. The twin thickness measured in the present work ranges from 25 nm to 100 nm. The measured twin thickness is larger than that reported for high Mn TWIP steels (Kim and De Cooman, 2016) and the $Al_{0.1}$CoCrFeNi alloy (Choudhuri et al., 2018) having similar SFE. Especially, Choudhuri et al. (2018) reported the occurrence of nanoscale (~2 nm thickness) deformation twins upon deformation of the $Al_{0.1}$CoCrFeNi alloy. A decrease of deformation twin thickness with decreasing SFE was reported for CuAl alloys (Zhang et al., 2009), high Mn TWIP steels (Kim and De Cooman, 2016; Yang et al., 2013), and HEAs (Liu et al., 2018). Thinner deformation twins would result in more interfaces between matrix and deformation twins, which could reduce the mean free path of dislocations and enhance

the dynamic Hall-Petch effect and the strain hardening capacity of the material (Yang et al., 2013). Idrissi et al. (Idrissi et al., 2010b) compared the internal structure of deformation twins in the Fe-Mn-C and Fe-Mn-Si-Al TWIP steels and reported thin deformation twins with a high density of sessile dislocations in the Fe-Mn-C TWIP steels. The sessile dislocations were identified as Frank partial dislocations in the twinning plane, which could hinder the movement of Shockley partial dislocations and contribute to the high work hardening of the Fe-Mn-C TWIP steels (Idrissi et al., 2010a; Kim et al., 2017). The sessile dislocations observed in twins of FCC materials result from a type of dislocation transmutation mechanisms referring to the change of slip plane and Burgers vector of a dislocation when incorporated into a twin (El Kadiri and Oppedal, 2010; Niewczas, 2010; Wang and Agnew, 2016). So far, no in-depth analysis of such dislocations is available for HEAs.

To enhance the strain hardening capacity of HEAs, thin deformation twins with sessile dislocations present at twin/matrix interfaces would be beneficial. The effect of chemical composition on the structure of deformation twins would be an interesting topic for future research. For example, the cold-rolled $Fe_{50}Mn_{30}Co_{10}Cr_{10}$ HEA micro-alloyed with nitrogen showed deformation twin thickness of 10 nm (He et al., 2021b), thinner than the twin thickness measured in the present work.

4.4. Various deformation mechanisms activated upon subzero deformation

In contrast to the room temperature deformation, deformation at 223 K leads to the activation of the deformation-induced HCP phase. The observed dislocation structures at room temperature and 223 K are similar except for the activation of different types of plasticity enhancing mechanisms, i.e. deformation twinning at room temperature and deformation-induced HCP martensitic transformation at 223 K.

The hardening effect by deformation-induced HCP martensitic transformation was observed in previous works of FeMn based alloys (O. Grassel, 2000; Tomota et al., 1986). The deformation-induced HCP martensitic transformation could contribute to the hardening of the material since the interfaces between the HCP phase and the matrix could act as barriers for dislocation motion and reduce the mean free path of dislocations (Wong et al., 2016). The present results are consistent with other materials exhibiting deformation-induced HCP martensitic transformation, which generally show higher strain hardening capacity than the materials exhibiting the TWIP effect (Frommeyer et al., 2003; Tomota et al., 1986).

At the high deformation level near the fracture surface, kink banding and reverse transformation are activated in addition to deformation-induced HCP martensitic transformation. Kink banding mechanisms have been observed in materials exhibiting extensive slip but on a limited number of easy glide systems (Barsoum et al., 2003). Such materials generally show a high c/a ratio and the representative examples include the ternary $M_{n+1}AX_n$ compound such as Ti_3SiC_2 (Barsoum et al., 2003), Zn single crystals loaded parallel to their basal plane (Orowan, 1942), and Mg alloys with long-period stacking ordered structures (Kim et al., 2015). Although precise kink banding mechanisms have not been identified, confinement of dislocations on easy glide planes such as the basal plane, the formation of dislocation boundaries normal to the easy glide plane, and the accommodation of the misorientation across the kink boundaries could be the key processes. The deformation-induced HCP phase observed in the investigated material could easily activate basal slip as observed in the HCP phase of the $Fe_{50}Mn_{30}Co_{10}Cr_{10}$ alloy (Bu et al., 2019). The rotation of the $(0002)_{HCP}$ // $(1\bar{1}1)_{FCC}$ plane by 12 ° (Fig. 13(a)) suggests the presence of kink boundaries normal to the basal plane, and the kink boundaries are expected to be formed by accommodation of basal dislocations as reported in previous works (Hagihara et al., 2016; Kim et al., 2015). The formation of kink bands could contribute to the accommodation of the ⟨c⟩ axis deformation (Kim et al., 2015), thereby contributing to the ductility of the material upon subzero deformation.

Reverse transformed FCC bands were observed in the region of highly dense deformation-induced HCP structures (Fig. 13. (b) and (c)). The reverse transformation from HCP to FCC is expected to contribute to stress relaxation at the regions having extremely high defect density, and also enhancement of local strain hardenability due to the high defect density within the transformed FCC bands (Wei et al., 2020). The observed characteristic deformation mechanisms of kink banding and reverse transformation are related to the highly dense deformation-induced HCP structures, and both the mechanisms could contribute to the strain accommodation and the stress relaxation, leading to the large ductility during subzero deformation.

5. Conclusions

We present the mechanical properties and deformation mechanisms of the cold-rolled and annealed $Fe_{40}Mn_{40}Co_{10}Cr_{10}$ alloy, both at room temperature (298 K) and subzero temperature (223 K). The material deformed at 223 K shows a higher strain hardening rate than the material deformed at 298 K. The main deformation mechanisms of the investigated HEA include the development of inhomogeneous dislocation structures and interaction between dislocations and deformation twin/mechanically induced HCP martensite. The stacking fault energy measured using TEM weak-beam dark-field imaging of dissociated dislocations is 20 ± 9 mJ/m^2 at 298 K. The $Fe_{40}Mn_{40}Co_{10}Cr_{10}$ alloy exhibiting a positive temperature dependence of SFE leads to a decrease of SFE as deformation temperature decreases from 298 K to 223 K. The decrease of SFE results in the transition from deformation twinning to deformation-induced HCP transformation. Further, at higher strains at 223 K, kink banding of HCP and reverse transformation from HCP to FCC were observed, which could account for strain accommodation and stress relaxation, and the large ductility. The 298 K deformation leads to various types of dislocation structures: Extended dislocations, Taylor lattice of perfect dislocations, dislocation loops, highly dense dislocation walls, cell blocks, and cell structures. The observed dislocation structures at 298 K and 223 K are similar suggesting the minor effect of SFE on dislocation structures. Investigations on the temperature-dependent dislocation structures of various FCC materials, including subzero temperatures and low SFE materials, are essential to verify the universality of the present observations.

CRediT authorship contribution statement

Jin-Kyung Kim: Conceptualization, Investigation, Writing – original draft, Writing – review & editing, Supervision. **Ji Hoon Kim:** Investigation. **Hyojin Park:** Investigation. **Jin-Seob Kim:** Investigation. **Guanghui Yang:** Investigation. **Rosa Kim:** Investigation. **Taejin Song:** Investigation. **Dong-Woo Suh:** Writing – review & editing, Supervision. **Jongryoul Kim:** Supervision.

Declaration of Competing Interest

The authors declare that they have no known competing financial interests or personal relationships that could have appeared to influence the work reported in this paper.

Acknowledgement

This research was supported by the Basic Science Research Program through the National Research Foundation of Korea funded by the Ministry of Education (2018R1D1A1B07044731), NRF-2021R1F1A1046001, and by Korea Institute for Advancement of Technology(KIAT) grant funded by the Korea Government(MOTIE) (P0002019, Human Resource Development Program for Industrial Innovation).

References

Aerts, E., Delavignette, P., Siems, R., Amelinckx, S., 1962. Stacking fault energy in silicon. J. Appl. Phys. 33, 3078–3080.
Allain, S., Chateau, J.P., Bouaziz, O., Migot, S., Guelton, N., 2004. Correlations between the calculated stacking fault energy and the plasticity mechanisms in Fe–Mn–C alloys. Mater. Sci. Eng. 387-389, 158–162.
Asgari, S., El-Danaf, E., Kalidindi, S.R., Doherty, R.D., 1997. Strain hardening regimes and microstructural evolution during large strain compression of low stacking fault energy fcc alloys that form deformation twins. Metall. Mater. Trans. A 28, 1781–1795.
Barsoum, M.W., Zhen, T., Kalidindi, S.R., Radovic, M., Murugaiah, A., 2003. Fully reversible, dislocation-based compressive deformation of Ti3SiC2 to 1GPa. Nat. Mater. 2, 107–111.
Bouaziz, O., Allain, S., Scott, C., 2008. Effect of grain and twin boundaries on the hardening mechanisms of twinning-induced plasticity steels. Scr. Mater. 58, 484–487.
Bu, Y., Li, Z., Liu, J., Wang, H., Raabe, D., Yang, W., 2019. Nonbasal slip systems enable a strong and ductile hexagonal-close-packed high-entropy phase. Phys. Rev. Lett. 122, 075502.
Canadinc, D., Sehitoglu, H., Maier, H.J., Chumlyakov, Y.I., 2005. Strain hardening behavior of aluminum alloyed Hadfield steel single crystals. Acta Mater. 53, 1831–1842.
Canadinc, D., Sehitoglu, H., Maier, H.J., Niklasch, D., Chumlyakov, Y.I., 2007. Orientation evolution in Hadfield steel single crystals under combined slip and twinning. Int. J. Solids Struct. 44, 34–50.
Chandan, A.K., Tripathy, S., Ghosh, M., Chowdhury, S.G., 2019. Evolution of substructure of a non-equiatomic FeMnCrCo high entropy alloy deformed at ambient temperature. Metall. Mater. Trans. A 50, 5079–5090.
Chandan, A.K., Tripathy, S., Sen, B., Ghosh, M., Ghosh Chowdhury, S., 2021. Temperature dependent deformation behavior and stacking fault energy of Fe40Mn40Co10Cr10 alloy. Scr. Mater. 199.
Choudhuri, D., Komarasamy, M., Ageh, V., Mishra, R.S., 2018. Investigation of plastic deformation modes in Al0.1CoCrFeNi high entropy alloy. Mater. Chem. Phys. 217, 308–314.
Churchman, A.T., 1955. The yield phenomena, kink bands and geometric softening in titanium crystals. Acta Metall. 3, 22–29.
Deng, Y., Tasan, C.C., Pradeep, K.G., Springer, H., Kostka, A., Raabe, D., 2015. Design of a twinning-induced plasticity high entropy alloy. Acta Mater. 94, 124–133.
El Kadiri, H., Oppedal, A.L., 2010. A crystal plasticity theory for latent hardening by glide twinning through dislocation transmutation and twin accommodation effects. J. Mech. Phys. Solids 58, 613–624.
Frommeyer, G., Brüx, U., Neumann, P., 2003. Supra-ductile and high-strength manganese-TRIP/TWIP steels for high energy absorption purposes. ISIJ Int. 43, 438–446.
George, E.P., Curtin, W.A., Tasan, C.C., 2020. High entropy alloys: a focused review of mechanical properties and deformation mechanisms. Acta Mater. 188, 435–474.
George, E.P., Raabe, D., Ritchie, R.O., 2019. High-entropy alloys. Nat. Rev. Mater. 4, 515–534.
Gludovatz, B., Hohenwarter, A., Catoor, D., Chang, E.H., George, E.P., Ritchie, R.O., 2014. A fracture-resistant high-entropy alloy for cryogenic applications. Science 345, 1153–1158.
Gutierrez-Urrutia, I., Raabe, D., 2011. Dislocation and twin substructure evolution during strain hardening of an Fe–22wt.% Mn–0.6wt.% C TWIP steel observed by electron channeling contrast imaging. Acta Mater. 59, 6449–6462.
Gutierrez-Urrutia, I., Raabe, D., 2012. Multistage strain hardening through dislocation substructure and twinning in a high strength and ductile weight-reduced Fe–Mn–Al–C steel. Acta Mater. 60, 5791–5802.
Hagihara, K., Mayama, T., Honnami, M., Yamasaki, M., Izuno, H., Okamoto, T., Ohashi, T., Nakano, T., Kawamura, Y., 2016. Orientation dependence of the deformation kink band formation behavior in Zn single crystal. Int. J. Plast. 77, 174–191.
He, F., Yang, Z., Liu, S., Chen, D., Lin, W., Yang, T., Wei, D., Wang, Z., Wang, J., Kai, J.-j., 2021a. Strain partitioning enables excellent tensile ductility in precipitated heterogeneous high-entropy alloys with gigapascal yield strength. Int. J. Plast. 144.
He, Z., Jia, N., Yan, H., Shen, Y., Zhu, M., Guan, X., Zhao, X., Jin, S., Sha, G., Zhu, Y., Liu, C.T., 2021b. Multi-heterostructure and mechanical properties of N-doped FeMnCoCr high entropy alloy. Int. J. Plast. 139.
He, Z.F., Jia, N., Ma, D., Yan, H.L., Li, Z.M., Raabe, D., 2019. Joint contribution of transformation and twinning to the high strength-ductility combination of a FeMnCoCr high entropy alloy at cryogenic temperatures. Mater. Sci. Eng. 759, 437–447.
Hong, S.I., Laird, C., 1990. Mechanisms of slip mode modification in F.C.C. solid solutions. Acta Metall. Mater. 38, 1581–1594.
Huang, S., Li, W., Lu, S., Tian, F., Shen, J., Holmström, E., Vitos, L., 2015. Temperature dependent stacking fault energy of FeCrCoNiMn high entropy alloy. Scr. Mater. 108, 44–47.
Huang, S., Huang, H., Li, W., Kim, D., Lu, S., Li, X., Holmström, E., Kwon, S.K., Vitos, L., 2018. Twinning in metastable high-entropy alloys. Nat. Commun. 9, 2381.
Huo, W., Fang, F., Zhou, H., Xie, Z., Shang, J., Jiang, J., 2017. Remarkable strength of CoCrFeNi high-entropy alloy wires at cryogenic and elevated temperatures. Scr. Mater. 141, 125–128.
Idrissi, H., Renard, K., Ryelandt, L., Schryvers, D., Jacques, P.J., 2010a. On the mechanism of twin formation in Fe–Mn–C TWIP steels. Acta Mater. 58, 2464–2476.
Idrissi, H., Renard, K., Schryvers, D., Jacques, P.J., 2010b. On the relationship between the twin internal structure and the work-hardening rate of TWIP steels. Scr. Mater. 63, 961–964.

Jiang, L., Lu, Y.P., Song, M., Lu, C., Sun, K., Cao, Z.Q., Wang, T.M., Gao, F., Wang, L.M., 2019. A promising CoFeNi2V0.5Mo0.2 high entropy alloy with exceptional ductility. Scr. Mater. 165, 128–133.
Joo, S.H., Kato, H., Jang, M.J., Moon, J., Tsai, C.W., Yeh, J.W., Kim, H.S., 2017. Tensile deformation behavior and deformation twinning of an equimolar CoCrFeMnNi high-entropy alloy. Mater. Sci. Eng. 689, 122–133.
Kaushik, L., Kim, M.-S., Singh, J., Kang, J.-H., Heo, Y.-U., Suh, J.-Y., Choi, S.-H., 2021. Deformation mechanisms and texture evolution in high entropy alloy during cold rolling. Int. J. Plast. 141.
Kim, J.-K., De Cooman, B.C., 2016. Stacking fault energy and deformation mechanisms in Fe-xMn-0.6C-yAl TWIP steel. Mater. Sci. Eng. 676, 216–231.
Kim, J.-K., Kwon, M.-H., De Cooman, B.C., 2017. On the deformation twinning mechanisms in twinning-induced plasticity steel. Acta Mater. 141, 444–455.
Kim, J.-K., Sandlöbes, S., Raabe, D., 2015. On the room temperature deformation mechanisms of a Mg–Y–Zn alloy with long-period-stacking-ordered structures. Acta Mater. 82, 414–423.
Kim, J., Estrin, Y., De Cooman, B.C., 2013. Application of a dislocation density-based constitutive model to Al-alloyed TWIP steel. Metall. Mater. Trans. A 44, 4168–4182.
Kuhlmann-Wilsdorf, D., 1989. Theory of Plastic Deformation:– properties of low energy dislocation structures. Mater. Sci. Eng. 113, 1–41.
Remy, L., Pineau, A., 1977. Twinning and strain-induced FCC-HCP transformation in the Fe-Mn-Cr-C system. Mater. Sci. Eng. 28, 99–107.
Landau, P., Makov, G., Shneck, R.Z., Venkert, A., 2011. Universal strain–temperature dependence of dislocation structure evolution in face-centered-cubic metals. Acta Mater. 59, 5342–5350.
Laplanche, G., Kostka, A., Horst, O.M., Eggeler, G., George, E.P., 2016. Microstructure evolution and critical stress for twinning in the CrMnFeCoNi high-entropy alloy. Acta Mater. 118, 152–163.
Li, Z., Pradeep, K.G., Deng, Y., Raabe, D., Tasan, C.C., 2016. Metastable high-entropy dual-phase alloys overcome the strength-ductility trade-off. Nature 534, 227–230.
Li, Z., Raabe, D., 2017. Strong and ductile non-equiatomic high-entropy alloys: design, processing, microstructure, and mechanical properties. JOM 69, 2099–2106, 1989.
Li, Z., Tasan, C.C., Pradeep, K.G., Raabe, D., 2017. A TRIP-assisted dual-phase high-entropy alloy: grain size and phase fraction effects on deformation behavior. Acta Mater. 131, 323–335.
Liu, S.F., Wu, Y., Wang, H.T., He, J.Y., Liu, J.B., Chen, C.X., Liu, X.J., Wang, H., Lu, Z.P., 2018. Stacking fault energy of face-centered-cubic high entropy alloys. Intermetallics 93, 269–273.
Lu, W., Liebscher, C.H., Dehm, G., Raabe, D., Li, Z., 2018. Bidirectional transformation enables hierarchical nanolaminate dual-phase high-entropy alloys. Adv. Mater. 30, e1804727.
Ma, D., Yao, M., Pradeep, K.G., Tasan, C.C., Springer, H., Raabe, D., 2015. Phase stability of non-equiatomic CoCrFeMnNi high entropy alloys. Acta Mater. 98, 288–296.
Ma, E., 2020. Unusual dislocation behavior in high-entropy alloys. Scr. Mater. 181, 127–133.
Mahajan, S., Pande, C.S., Imam, M.A., Rath, B.B., 1997. Formation of annealing twins in f.c.c. crystals. Acta Mater. 45, 2633–2638.
Ming, K., Bi, X., Wang, J., 2018. Realizing strength-ductility combination of coarse-grained Al0.2Co1.5CrFeNi1.5Ti0.3 alloy via nano-sized, coherent precipitates. Int. J. Plast. 100, 177–191.
Ming, K., Bi, X., Wang, J., 2019. Strength and ductility of CrFeCoNiMo alloy with hierarchical microstructures. Int. J. Plast. 113, 255–268.
Niewczas, M., 2010. Lattice correspondence during twinning in hexagonal close-packed crystals. Acta Mater. 58, 5848–5857.
Grassel, O., Krüger, L., Frommeyer, G., Meyer, L.W., 2000. High strength Fe-Mn-(Al,Si) TRIP/TWIP steels development-properties-application. Internatinal Journal of Plasticity 16, 1391–1409.
Olson, G.B., Cohen, M., 1976. A general mechanism of martensitic nucleation: Part I. General concepts and the FCC-HCP transformation. Metall. Trans. A 7, 1897–1904.
Orowan, E., 1942. A type of plastic deformation new in metals. Nature 149, 643–644.
Otto, F., Dlouhý, A., Somsen, C., Bei, H., Eggeler, G., George, E.P., 2013. The influences of temperature and microstructure on the tensile properties of a CoCrFeMnNi high-entropy alloy. Acta Mater. 61, 5743–5755.
Picak, S., Liu, J., Hayrettin, C., Nasim, W., Canadinc, D., Xie, K., Chumlyakov, Y.I., Kireeva, I.V., Karaman, I., 2019. Anomalous work hardening behavior of Fe40Mn40Cr10Co10 high entropy alloy single crystals deformed by twinning and slip. Acta Mater. 181, 555–569.
Pradeep, K.G., Tasan, C.C., Yao, M.J., Deng, Y., Springer, H., Raabe, D., 2015. Non-equiatomic high entropy alloys: approach towards rapid alloy screening and property-oriented design. Mater. Sci. Eng. 648, 183–192.
Schneider, M., George, E.P., Manescau, T.J., Záležák, T., Hunfeld, J., Dlouhý, A., Eggeler, G., Laplanche, G., 2020. Analysis of strengthening due to grain boundaries and annealing twin boundaries in the CrCoNi medium-entropy alloy. Int. J. Plast. 124, 155–169.
Shih, M., Miao, J., Mills, M., Ghazisaeidi, M., 2021. Stacking fault energy in concentrated alloys. Nat. Commun. 12, 3590.
Steinmetz, D.R., Jäpel, T., Wietbrock, B., Eisenlohr, P., Gutierrez-Urrutia, I., Saeed–Akbari, A., Hickel, T., Roters, F., Raabe, D., 2013. Revealing the strain-hardening behavior of twinning-induced plasticity steels: theory, simulations, experiments. Acta Mater. 61, 494–510.
Steve, 2000. Accurate quantitative analysis of clay and other minerals in sandstones by XRD: comparison of a Rietveld and a reference intensity ratio (RIR) method and the importance of sample preparation. Clay Miner. 35, 291–302.
Su, J., Wu, X., Raabe, D., Li, Z., 2019. Deformation-driven bidirectional transformation promotes bulk nanostructure formation in a metastable interstitial high entropy alloy. Acta Mater. 167, 23–39.
Tomota, Y., Strum, M., Morris, J.W., 1986. Microstructural dependence of Fe-high Mn tensile behavior. Metall. Trans. A 17, 537–547.
Wang, F., Agnew, S.R., 2016. Dislocation transmutation by tension twinning in magnesium alloy AZ31. Int. J. Plast. 81, 63–86.
Wang, Z., Wang, C., Zhao, Y.-L., Hsu, Y.-C., Li, C.-L., Kai, J.-J., Liu, C.-T., Hsueh, .C..-H., 2020. High hardness and fatigue resistance of CoCrFeMnNi high entropy alloy films with ultrahigh-density nanotwins. Int. J. Plast. 131.
Wei, S., Kim, J., Cann, J.L., Gholizadeh, R., Tsuji, N., Tasan, C.C., 2020. Plastic strain-induced sequential martensitic transformation. Scr. Mater. 185, 36–41.
Williams, D.B., Carter, C.B., 1996. Transmission Electron Microscopy. Plenum Press, New York.
Winther, G., Jensen, D.J., Hansen, N., 1997. Dense dislocation walls and microbands aligned with slip planes- theoretical considerations. Acta Mater. 45, 5059–5068.
Wong, S.L., Madivala, M., Prahl, U., Roters, F., Raabe, D., 2016. A crystal plasticity model for twinning- and transformation-induced plasticity. Acta Mater. 118, 140–151.
Wu, S.W., Wang, G., Wang, Q., Jia, Y.D., Yi, J., Zhai, Q.J., Liu, J.B., Sun, B.A., Chu, H.J., Shen, J., Liaw, P.K., Liu, C.T., Zhang, T.Y., 2019. Enhancement of strength-ductility trade-off in a high-entropy alloy through a heterogeneous structure. Acta Mater. 165, 444–458.
Xu, X.D., Liu, P., Tang, Z., Hirata, A., Song, S.X., Nieh, T.G., Liaw, P.K., Liu, C.T., Chen, M.W., 2018. Transmission electron microscopy characterization of dislocation structure in a face-centered cubic high-entropy alloy Al0.1CoCrFeNi. Acta Mater. 144, 107–115.
Yang, H.K., Zhang, Z.J., Zhang, Z.F., 2013. Comparison of work hardening and deformation twinning evolution in Fe–22Mn–0.6C–(1.5Al) twinning-induced plasticity steels. Scr. Mater. 68, 992–995.
Yang, T., Zhao, Y.L., Tong, Y., Jiao, Z.B., Wei, J., Cai, J.X., Han, X.D., Chen, D., Hu, A., Kai, J.J., Lu, K., Liu, Y., Liu, C.T., 2018. Multicomponent intermetallic nanoparticles and superb mechanical behaviors of complex alloys. Science 362, 933–937.
Yao, M.J., Pradeep, K.G., Tasan, C.C., Raabe, D., 2014. A novel, single phase, non-equiatomic FeMnNiCoCr high-entropy alloy with exceptional phase stability and tensile ductility. Scr. Mater. 72-73, 5–8.
Zaddach, A.J., Niu, C., Koch, C.C., Irving, D.L., 2013. Mechanical properties and stacking fault energies of NiFeCrCoMn high-entropy alloy. JOM 65, 1780–1789.
Zhang, T.W., Ma, S.G., Zhao, D., Wu, Y.C., Zhang, Y., Wang, Z.H., Qiao, J.W., 2020. Simultaneous enhancement of strength and ductility in a NiCoCrFe high-entropy alloy upon dynamic tension: micromechanism and constitutive modeling. Int. J. Plast. 124, 226–246.
Zhang, Y., Tao, N.R., Lu, K., 2009. Effect of stacking-fault energy on deformation twin thickness in Cu–Al alloys. Scr. Mater. 60, 211–213.